Bachelorarbeit

# Dynamic Modelling of a modular robot finger

## Bachelorarbeit

Andreas Meißner

DLR

| Institut für Robotik und Mechatronik | BJ.: 2014 |
|---|---|
| | IB.Nr.: 572-14-13 |

# BACHELORARBEIT

# DYNAMIC MODELLING OF A MODULAR ROBOT FINGER

| Freigabe: | Der Bearbeiter: | Unterschriften |
|---|---|---|
| | Andreas Meißner | |
| | Betreuer: | |
| | Neal Yi-Sheng Lii | |
| | Der Institutsdirektor | |
| | Dr. Alin Albu-Schäffer | |

Dieser Bericht enthält 104 Seiten, 41 Abbildungen und 4 Tabellen

| Ort: Oberpfaffenhofen | Datum: 02.06.2014 | Bearbeiter: Meißner Andreas | Zeichen: |
|---|---|---|---|



Bachelor Thesis

# Dynamic Modelling of a modular robot finger

*Supervisors:*
Dr. Neal Y. Lii
Dr. Zhaopeng Chen

*Author:*
Andreas Meissner

*Examiners:*
Prof. Dr.-Ing. Alexander Steinkogler
Prof. Dr. rer. nat. Alfred Kersch

*A thesis submitted in fulfilment of the requirements for the degree of Bachelor of Science*

*in the*

University of Applied Sciences Munich
Department of Applied Sciences and Mechatronics

June 2014

UNIVERSITY OF APPLIED SCIENCES MUNICH

# *Abstract*

Department of Applied Sciences and Mechatronics

Bachelor of Science

**Dynamic Modelling of a modular robot finger**

by Andreas Meissner

New generations of dexterous robotic hands with high degrees of freedom, integrated advanced sensors, improving power-to-weight ratio, have shown great potential for performing complex tasks beyond simple grasping such as manipulation and gaiting. With the help of control strategies such as impedance and compliance control, together with various compensation methods, researchers have achieved some success in performing dexterous tasks with robotic hands. However, the lack of a dynamic model of the robotic hand has placed an inherent limitation on their dexterous performance.

The goal of this work is to address this omission to help eliminate this control performance limitation by deducing a dynamic model for one of the more successful and established dexterous robotic hands available today: the DLR/HIT Hand II. This robotic hand consists of five identical modular fingers, each finger has three degrees of freedom with dedicated position sensors and force-torque sensors at every joint. As a result of its identical modularity, it is sufficient to model one finger to be extended to five fingers to obtain the model of the hand.

Model based control is used in many applications in robotics, including the closely related robotic arms. However, for anthropomorphic robot hands little research is available. The contribution of this work is to create a complete model including a characterization of the motors to find the relationship between the control signal and the produced torque, the effects of friction in all the components, and the influence of the dynamics such as mass matrix, centrifugal term and gravitation. Furthermore, as the friction differs from finger to finger and the parameters may change over time, an algorithm to adjust the friction model is proposed in this work.

## Kurzfassung

Neue Generationen fingerfertiger Roboterhände mit einer hohen Anzahl an Freiheitsgraden, integrierten hoch entwickelten Sensoren und sich verbesserndem Kraft zu Gewicht Verhältnis, haben großes Potenzial bei der Ausführung komplexer Aufgaben wie der Manipulation gezeigt. Diese gehen über das einfache Greifen hinaus. Durch den Einsatz von Regelungsstrategien wie Impedanz- und Nachgiebigkeitsregelung, kombiniert mit unterschiedlichen Kompensationsverfahren, haben Forscher einigen Erfolg in der Ausführung von fingerfertigen Aufgaben mit Roboterhänden erreicht. Allerdings sorgt das Fehlen eines dynamischen Modells für eine inhärente Beschränkung der Geschicklichkeit.

Das Ziel dieser Arbeit ist diese Lücke in Angriff zu nehmen, um dabei zu helfen, diese Regelungsbeschränkung zu beseitigen. Dies wird durch die Herleitung eines dynamischen Modells für eine der erfolgreicheren und etablierten fingerfertigen Roboterhände, die heutzutage zur Verfügung stehen erreicht. Die DLR/HIT Hand II. Diese Roboterhand besteht aus fünf identischen modularen Fingern. Jeder Finger hat drei Freiheitsgrade mit Positions- sowie Kraft-Drehmoment-Sensoren in jedem Gelenk. Durch die identische Modularität, ist es ausreichend, einen Finger zu modellieren und dieses Modell auf die ganze Hand zu erweitern.

Modellbasierte Regelung wird in vielen Anwendungsgebieten der Robotik, wie den eng verwandten Roboterarmen verwendet. Allerdings ist für anthropomorphe Roboterhände wenig Forschungsarbeit verfügbar. Der Beitrag dieser Arbeit ist die Erstellung eines vollständigen Modells, einschließlich einer Charakterisierung der Motoren um die Beziehung zwischen Steuerungssignal und produziertem Drehmoment, die Reibung in allen Bauteilen und den Einfluss der Dynamik wie Massenmatrix, Zentrifugalterm sowie Gravitation zu bestimmen. Da die Reibung von Finger zu Finger abweicht, wird ein Algorithmus für die Anpassung des Reibungsmodells in dieser Arbeit vorgeschlagen.

# *Acknowledgements*

I would like to express the deepest appreciation to my supervising professor Prof. Dr. Ing. Alexander Steinkogler for his patience, encouragement and ideas on the improvement of the model. I would like to especially thank my research group. Deepest gratitude to Neal Lii, Zhaopeng Chen and Benedikt Pleintinger for their constant support. Without their encouragement and suggestion this thesis would not have been possible. I am deeply grateful to Natalia Irigoyen and Annika Maier for their help with constructing the testbed. I wish to acknowledge the valueable discussions with Aaron Pereira.

I appreciate the advice about the dynamics given by Dr. Thomas Wimböck, which helped me a lot. Furthermore, I thank my second supervising professor Prof. Dr. rer. nat. Alfred Kersch, who supported me in the completion of the thesis.

In addition, I offer my regards and blessings to my proofreaders for their comments and suggestions and all of those, who supported me in every respect during the completion of the project.

# Contents

# List of Figures

# List of Tables

# Symbols

| Symbol | Name | Unit |
|---|---|---|
| F | Cartesian force | N |
| $\Delta$x | Cartesian position | m |
| $M_I$ | Virtual inertia | $N{\cdot}s^2/m$ |
| $D_k$ | damping | $N{\cdot}s/m$ |
| $K_k$ | stiffness | N/m |
| ${}^A_B\mathbf{R}$ | Rotation Matrix from A to B | |
| ${}^A_B\mathbf{T}$ | Transformation Matrix from frame A to B | |
| $\mathbf{p}$ | position vector | |
| $\hat{\mathbf{z}}_i$ | vector of joint axis i | |
| $\hat{\mathbf{x}}_i$ | vector of coordinate axis x | |
| $\hat{\mathbf{y}}_i$ | vector of coordinate axis y | |
| $d_i$ | link offset of joint i | |
| $\alpha_i$ | link twist | |
| $\tau$ | torque | Nm |
| $\theta$ | angle | $^\circ$ |
| $\omega$ | angular frequency | rad/s |
| $M(\theta, \ddot{\theta})$ | Mass term | Nm |
| $M\_i$ | inertia of joint i | kg $\cdot m^2$ |
| $M\_i\_rest$ | remaining Mass term | Nm |
| $C(\theta, \dot{\theta})$ | centrifugal term | Nm |
| $G(\theta)$ | gravitational term | Nm |
| $P_{el}$ | electrical power | W |
| $P_{mech}$ | mechanical power | W |
| $P_J$ | thermal power | W |
| $P_F$ | friction loss | W |
| T | temperature | K |
| U | voltage | V |
| I | current | A |

| | | |
|---|---|---|
| R | resistance | Ω |
| n | rotational speed | rpm |
| $\alpha_T$ | temperature coefficient | 1/K |
| PWM | pulse width modulation signal | |
| b | slope of motor torque over motor velocity | |
| a | slope of motor torque over PWM signal | |
| $F_F(\theta, \dot{\theta})$ | Friction Term | Nm |
| $F_C$ | Coulomb Friction | |
| $F_N$ | Normal Force | N |
| $F_S$ | stiction | |
| $\sigma$ | viscous coefficient | |
| $\mu$ | Coulomb Friction coefficient | |
| $\mu_h$ | stiction coefficient | |
| $V_S$ | Stribeck–velocity | |
| $\delta$ | Stribeck–shape–factor | |

# Abbreviations

| | |
|---|---|
| **EVA** | **E**xtra- **V**ehicular **A**ctivity |
| **DLR** | **D**eutsches Zentrum für **L**uft- und **R**aumfahrt |
| **HIT** | **H**arbin **I**nstitute of **T**echnology |
| **IFR** | **I**nternational **F**ederation of **R**obotics |
| **DOF** | **D**egree **O**f **F**reedom |
| **BLDC** | **B**russ **L**ess **D**irect **Current** |
| **HD** | **H**armonic **D**rive |
| **HASy** | **H**and **A**rm **Sy**stem |
| **PIP** | **P**roximal **I**nter**p**halangeal joint |
| **DIP** | **D**istal **I**nter**p**halangeal joint |
| **BGA** | **B**all **G**rid **A**rray |
| **FPGA** | **F**ield **P**rogrammable **G**ate **Array** |
| **DSP** | **D**igital **S**ignal **P**rocessor |
| **PWM** | **P**ulse **W**idth **M**odulation |

# Chapter 1

# Introduction

Industrial robotics is already an important part of modern production and automation which continues to progress. The IFR Statistical Department expects that between 2014 and 2016 worldwide robot sales will increase yearly by about 6 % [1]. However, production and logistics are not the only applications. Robotics have found their way into many other fields. For example, nuclear power plants [2] and medical applications such as surgery, rehabilitation [3] or prosthetics [4] .

Many tasks currently performed by humans are dangerous and unhealthy. For example, in aerospace, in deep sea or in search and rescue tasks, accidents are often life-threatening. Due an ageing demographic, a huge gap in elder care is expected. Companies like Toyota are trying to get into these markets and are developing robots to support elder people and the care attendants [5].

For many tasks, such as mass production or surgery, robots are designed for a specific task. In production, robots mostly have a fixed position, no obstacles are in the workspace and the end effectors are also specialized for one task. The term end effector specifies a device or tool at the end of a robot arm.

In other applications like elder care, rescue tasks or space, robots have to work in unstructured environments where many different tasks have to be fulfilled. In order to adept to unexpected situations a multifunctional end effector is desired.

The environment in the modern world, as well as all kind of tools, are designed for the use of humans. Also the humanoid hand is one of the best manipulators nature has

created. A manipulator is the device which is used for interaction with the environment. So it is obviously to aim for a humanoid hand to create a multifunctional manipulator which is able to solve the same problems as humans. This has also the benefit of the intuitive use in teleoperation and prosthetics.

In teleoperation or telemanipulation the movement of a humanoid hand is captured with a dataglove and this data is used to control a robot hand [6]. Force feedback can also be implemented. The benefit of telemanipulation is to work in dangerous or not reachable areas without risks for a human and still have the creative mind which is the weakness of robots. For example, in space, an astronaut needs several hours of preparation before he can carry out extra vehicular activities (EVAs). Outside of the space station, critical situations like a damaged spacesuit can occur. To avoid these risks, a robot which is able to perform EVAs and can be controlled from inside of the station with an interface like the dataglove or from earth is helpful.

Unfortunately, technology has not come close to the performance of the humanoid hand. The humanoid hand consists of 27 bones and at least 23 degrees of freedom (DOF). [7] Although robotic designs approaching human DOF and force to weight ratio such as the DLR Hand Arm System (HASy) have been proposed recently [8], the control concepts and applications for achieving human level of dexterity remains with such mechanical designs a great challenge.

To achieve the goal of maximizing task capability with the current robotics technology, blindly mimicking the human form may not be the best solution. On the other hand, the robots can be designed for easy repair and replacement, which gives them an advantage over humans. Given that it is not likely in the near future to fully achieve human hand performance in a mechatronic/robotic design through mimicry, different approaches to design and control an end effector should be considered.

## 1.1 Motivation

In order to perform the same tasks as the human hand, two different objectives have to be fulfilled. The first is the ability to grasp different objects robustly and the second is to manipulate objects with different shapes. Especially manipulation requires precise control of position and force. Therefore, a variety of control concepts such as impedance

control [9], stiffness control [10] or compliance control [11] were developed. To improve the control performance or using model based control, an accurate model of the system is in great demand. This model characterizes ideally the output of the motor, behaviour of friction and transmission elements as well as the dynamics of the manipulator.

## 1.2 Anatomical terminology used in the following chapters

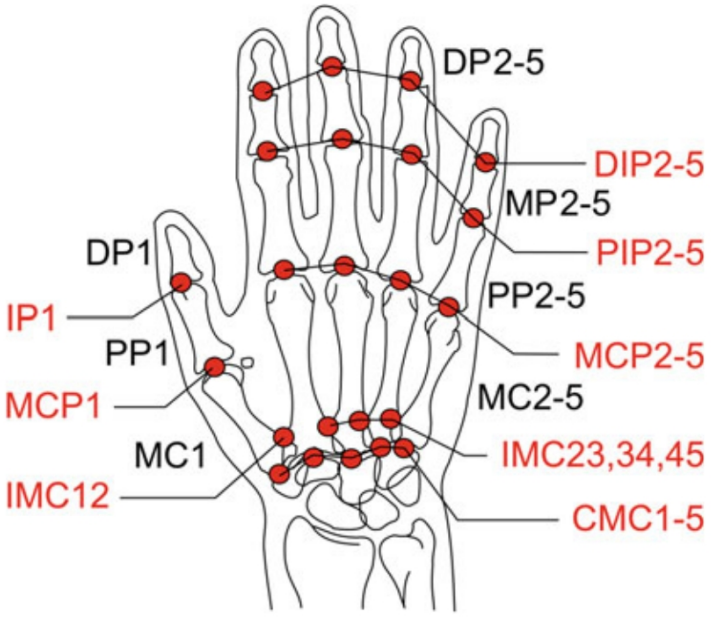


FIGURE 1.1: Anatomical terms of a human hand [7], distal joint is next to the fingertip, proximal joint in the middle of each finger and metacarpophalangeal joints specifies the joint in the knuckle

Given that this thesis is focused on anthropomorphic robot hands the following terms are used to describe the different parts of the hand.

- Distal phalanx (DP2-5) in figure 1.1
- Medial phalanx (MP2-5) in figure 1.1
- Proximal phalanx (PP2-5) in figure 1.1
- Metacarpophalangeal joints (MCP2-5) in figure 1.1
- Proximal interphalangeal joints (PIP2-5) in figure 1.1
- Distal interphalanges joints (DIP2-5) in figure 1.1

## 1.3 Dynamic robot modelling

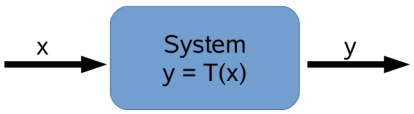


FIGURE 1.2: System with Input x and Output y

The goal of a dynamic model is to provide a more precise plant description to enable improvement of controller performance. To achieve this, the relationship between the input x and output y (see figure 1.2) should be obtained. Depending on the complexity and precision required by the control performance, elements such as active components (e.g. motor, actuators), mechanisms, structures, friction, temperature (including variance), can all be considered in deducing a suitable plant to be utilized with a controller design. Modelling of robotic manipulators have been performed in previous work [12]. However, the model target in previous work have been on larger robots. In comparison, the target system of end effectors and hands tend to be much smaller in size and carry with them more design complexity due to the need to house many components in a little amount of space

# Chapter 2

# State of the art in end effector design

This chapter includes different approaches for anthropomorphic robot hands. Of course the development of robotic hands also involves other concepts than anthropomorphic hands. For example jammable grippers like the VERSABALL [13] or microhands e.g. [14]. In the meantime so many different robot hands are developed, that it is impossible to mention everything worthwhile, appropriately in this thesis. Hence the following hands were chosen to give an overview about different concepts for anthropomorphic hands. The Elumotion ELU–2 Hand, EH1 Milano Hand, Shadow Robot Company's Dexterous Hand, the DLR Hand Arm System, DLR Dexhand, Robonaut 2 Hand, Gifu Hand series and DLR Hand II.

Generally there are two kinds of anthropomorphic hands. One is external actuated, where all the actuators are mounted in the forearm and the fingers are moved via tendons. However, using tendons as transfer elements causes some problems regarding the modelling [15]. Another approach is the internal actuation hand which needs no forearm and all the actuators and electronics are integrated into the fingers and palm.

The term underactuated is used in robotics for manipulators with more DOF than actuators. In the case of robot hands, this means a coupled movement via tendons or other linkages. However, research of our group is focused on manipulation and underactuation is a handicap for manipulation.

| | underactuated | external actuation | internal actuation | tendon driven | pneumatic actuation | motor actuation | modular | joint torque sensing | space qualified/able |
|---|---|---|---|---|---|---|---|---|---|
| ELU–2 Hand | x | | x | | | x | | | |
| Milano Hand | x | x | | x | | x | | | |
| Shadow Hand | | x | | x | x | x | | | |
| DLR HASy | | x | | x | | x | | | |
| Dexhand | | | x | x | | x | | | x |
| Robonaut 2 Hand | | x | | x | | x | | | x |
| Gifu series | | | x | | | x | | | |
| DLR Hand II | | | x | | | x | x | x | |
| DLR/HIT Hand II | | | x | | | x | x | x | |

TABLE 2.1: Overview of presented hands

An overview about the different concepts of the presented hands is given in table 2.1.

## 2.1 Elumotion ELU–2 Hand

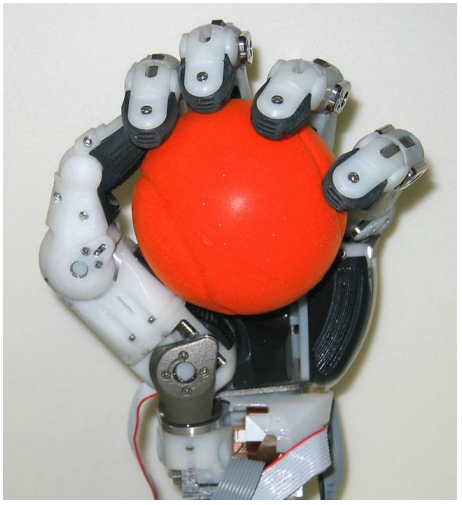

FIGURE 2.1: 9 DOF underactuated Elumotion ELU–2 Hand [16]: it weights 900 g and is capable of finger tip forces of up to 4.7 N

The Elu2–Hand [17] is a 9 DOF anthropomorphic robot hand with human scale. The servo actuators are within the hand's volume, which enables the possibility to fit the hand to different arms. The Elu2–Hand weighs 900 g, and is capable of finger tip forces of up to 4.7 N. The back–drivable finger transmissions enable the use of motor–current to indicate finger joint torque. In addition, the finger tips are equipped with force

sensors, which can help enable control schemes such as the aforementioned impedance and compliance control.

## 2.2 EH1 Milano Hand

FIGURE 2.2: underactuated 11 DOF EH1 Milano Hand [18] with passive compliance: it weights 1.4 kg and has a grasp payload of 5 kg

The passively compliant EH1 Milano Hand [18] has a weight of 1.4 kg with eleven DOFs and a grasp payload of 5 kg. Six Motors are embedded. Five flex/extend the fingers and the sixth is for abduction and adduction of the thumb's metacarpophalangeal joint.

Each finger has two phalanxes connected by means of two joints. The proximal phalanx (the closest to the palm) is made of aluminium whereas the distal phalanx (fingertip) is made of rubber. Each finger is actuated by means of a tendon that runs inside the phalanxes and is wrapped around the pulleys in the joints. While closing around an object the finger automatically adapts on the shape. This architecture promotes stability during precision or power grasps, which are by definition those grasps achieved by means of fingertips or palmar areas of the hand. The hand includes basic sensors for grasping and elementary manipulation. For all six motors, motor encoders for measuring the posture of the finger and current sensors to measure the produced torque respectively the grasping force are built in. Two proximity sensors per motor detect when the finger is fully flexed or extended. Additionally, five tendon tension force sensors are built

in. The motor encoders range between 0 (finger completely extended) and 255 (finger completely flexed). Due to different postures of the finger can still correspond to the same length of the tendon, it is not possible to measure the joint positions.

## 2.3 Shadow Hand

FIGURE 2.3: Dexterous Shadow Hand Motor driven on the left, pneumatic at the right [19]: it weights 4.2 kg and has 20 DOF

The Shadow Company's dexterous robot hand [20] combines a high degree of dexterity with considerable strength. Every finger has four DOFs, the thumb has an additional DOF, the palm and wrist have two. The Shadow Hand is available in two versions [19]. One version (E1M3) uses a electric actuation systems with integrated force– and position–control while the E1P1 uses pneumatic actuators with pressure as well as position control. The actuators are placed in the forearm. Hand and forearm have a total weight of 4.2 kg. Typical speeds are a full–range joint movement at frequencies of 1.0 Hz for the electric hand and 0.2 Hz for the pneumatic hand. A Hall effect sensor senses the rotation of each joint locally with typical resolution of 0.2 degrees. All Shadow hands have Pressure Sensor Tactiles fitted as standard in the fingertips. They are a single region sensor with high sensitivity and temperature compensation.

In the motor actuated hand a separate force sensor measures the force in each pair of tendons driven by the "Smart Motor unit" and is used locally for torque control. The data are also transmitted back to the PC. The sensors have a resolution of about 30 mN. One disadvantage is the space required for the compressor and actuators. Even if

the hand has the size of a humanoid hand, the required space in the forearm is huge and the weight high compared to other hands.

## 2.4 DLR hand Arm System

FIGURE 2.4: DLR Hand Arm System with variable stiffness actuation:It has a 19 DOF hand with 42 servo motors integrated in the forearm. Complete system [21] on the left, hand on the right [22]

If robotic systems operate in unstructured environments, collisions with objects are most likely inevitable. In cyclic tasks (e.g. running or bouncing) or in highly dynamic tasks (e.g. throwing), the actuators cannot provide sufficient forces during peak loads without getting too bulky and heavy. For this reason an anthropomorphic hand arm system [8] using variable stiffness actuation has been developed. The goal is to reach its human archetype regarding size, weight and performance. It has a 2–DOF wrist and 19–DOF hand with 42 servo motors integrated in the forearm. Each servo motor contains a position sensor. As the generated thermal energy exceeds the limits of typical air cooling system, a water cooling system is used. The main focus is put on robustness, dynamic performance and dexterity. Therefore, a paradigm change from impedance controlled, but mechanically stiff joints to robots using intrinsic variable compliance joints is carried out. Generally speaking, the energy introduced into the system, no matter whether caused by a collision, external forces or acceleration of the link inertia is converted to elastic energy. This power source can be used to regain kinetic energy and therefore enhance the dynamics of the system. Joint torque measurements are performed using the torque displacement relationship of the elastic elements in the joints. No further torque sensing device is necessary.

The wrist can rotate ±30° sideways, as well as ±90° for flexion/extension. It is designed to withstand 6.5 kN, i.e. the sum of the maximum tendon forces. Like human fingers, the index and middle finger have 4 DOF. The proximal and distal joint of the ring and fifth finger are coupled, to reduce the number of necessary actuators. The 5th DOF of the human thumb turned out to be of low relevance, and has been omitted. To ensure proper opposition of the thumb and the 5th finger, an antagonistically driven 4 bar mechanism was designed to mimic the motion of the fifth finger metacarpal bone (figure 1.1 MC1).

The interphalangeal joints on the other hand, are designed as hinge joints. All joints allow dislocation without damage in case of overload. In addition to robustness due to short–term energy storage, the use of antagonistic actuation enables to cope with tendon slackening or overstretching, which is one of the major problems of nowadays tendon–driven hands having inevitably constant tendon length. In contrast, antagonistic actuation is able to compensate unaligned pulley axes, and other geometrical errors via the elastic elements of the drive train. Therefore no explicit tendon tensioner is needed.

Impact tests have been performed, to verify the robustness of the DLR Hand Arm System. It has been hit with a 500 g hammer, while being in position control without any damage. As a first simple demonstration of the full system robustness, a nail has been driven into wood.

## 2.5 DLR Dexhand

The DLR Dexhand [24] consists of four modular fingers with 3 DOF each. This hand is designed to be able to perform a set of generic tasks with several EVA (extra vehicular activity) tools, e.g. pliers, cutter, brush, hammer, scoop, Allen wrench and pistol grip tools.

A disadvantage of the modularity is such that, if only one opposing finger is used, the thumb limits the maximum grasping force although the fingers on the other side would be able to produce a higher force. For this reason the thumb is a modified finger with at least a doubled finger tip force to increase the above mentioned capabilities. The active finger tip force is 25 N for a stretched finger, 100 N passively.

FIGURE 2.5: space qualify able tendon driven DLR Dexhand [23]

Polymer Dyneema tendons and harmonic drives are used, to bring the motor torque to the joints. All electronic parts are placed in the wrist which is protected by a 2 mm thick aluminium shell. This leads to a fully electromagnetically sealed design, with the exception of torque and temperature sensors. The aluminium shell also has the benefit of heat transfer and thermal inertia. Due to the absence of convective heat exchange in space, heat transfers are only the result of conduction and radiation. The hand control is based on three torque sensors per finger. As a result of the success of the ROKVISS experiment [25], which was conducted outer space for more than five years, with a robot design utilizing mostly standard automotive components, off–the–shelf solutions were employed for the Dexhand. However, in order to meet space qualification requirements, a human sized hand with 12 active joints is not feasible with exclusively radiation hardened parts.

## 2.6 Robonaut 2 Hand

The second generation Robonaut hand [27] has many advantages over its predecessor. This mechatronic device is more dexterous, has improved force control and sensing giving it the capability to grasp and actuate a wider range of tools. It can achieve peak forces of more than 20 N with a stretched finger and speeds of more than 200 mm/sec. Key to the hand's improved performance is the use of lower friction drive elements and a redistribution of components from the hand to the forearm, permitting more sensing in

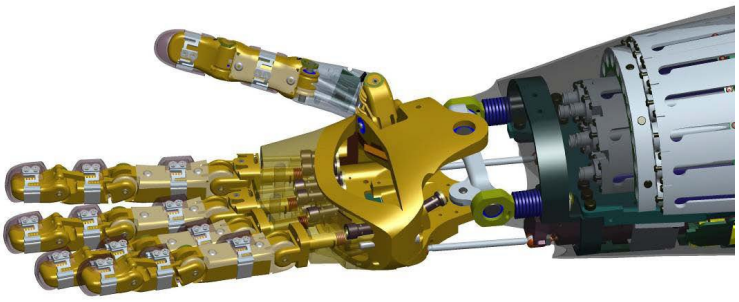

FIGURE 2.6: space qualified tendon driven Robonaut 2 Hand [26]

the fingers and palm. Sixteen finger actuators and two wrist actuators are placed in the forearm and yield a two DOF wrist as well as 12 DOFs to the hand.

The primary (index and middle) fingers have four independently controllable DOFs, the distal interphalangeal joint is connected to the proximal interphalangeal joint. The secondary fingers are mechanically similar to its primary fingers except the adduction / abduction of the base joint. They are underactuated and used primarily for grasping, as opposed to dexterous manipulation. For the tendons a hybrid weave of Teflon with Vectran is used. Such a tendon with diameter 1.2 mm has a break strength of 181 kg. Each actuator consists of a custom brushless DC motor with a hollow shaft which drives the nut of a ball screw. The screw extends and retracts a slider which drives a ball and socket linkage connected to the palm.

In the fingers and wrist three types of sensors are used. Measuring the absolute angular position of each joint is done by hall sensors. The proximal, medial, and distal phalanges of the fingers and the medial and distal phalanges of the thumb are each designed to accommodate a phalange tactile load cell, which is a novel six degree of freedom force torque sensor. Each load cell utilizes eight pairs of strain gauges mounted to an elastic aluminium element. Hard stops redirect the torque load if the applied force gets to big to ensure the strain element doesn't exceed its elastic limit.

## 2.7 Gifu Hand Series

The Gifu Hand series are 5–finger hands driven by built in servomotors that have 20 joints with 16 DOF. The thumb has 4 joints with 4 DOFs while the other fingers have 4

FIGURE 2.7: 16 DOF Gifu Hand III [28]

joints and 3 DOFs. Until now three versions are developed and all have the same design concept.

Gifu Hand I was used to investigate the hand's potential on dexterous grasping and manipulation [29], [30]. Due to the non negligible backlash in the gear transmissions, the hand was redesigned to reduce the backlash and enhance the output torque which resulted in Gifu Hand II [31]. Additionally to the six–axes force sensor at each fingertip a distributed tactile sensor with 624 detecting points was fixed on the surface of fingers and palm. Hand III followed this path and the backlash which appears after long operation was reduced and a new developed distributed tactile sensor with 859 detecting points in combination with a new real–time controller are used.

Hand III weights 1.4 kg and each servomotor is equipped with a magnetic encoder. The response of the fingers exceeds that of the human fingers and consequently the robot hand can move more quickly than the human hand. Use of satellite gearboxes and face gear in transmission leads to high stiffness and small backlash. The tactile sensor has grid pattern electrodes and uses conductive ink in which the electric resistance changes in proportion to the pressure on the top and bottom of a thin film. The maximum load is about 2.2 $\times 10^{-3} \mathrm{N/m^2}$. [28]

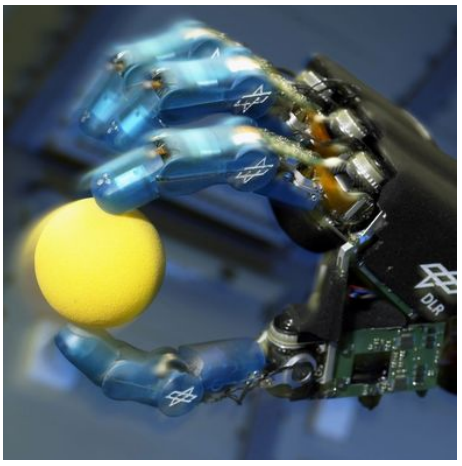


FIGURE 2.8: DLR Hand II [32] with modular fingers and local intelligence

## 2.8 DLR Hand II

The DLR Hand II [33] is the second generation of multi sensory hands developed at DLR with 13 DOF and an open skeleton structure for better maintenance and a automatically reconfigurable palm. Each identically modular finger is capable of a maximum tip force of 30N. All components are completely contained in the hand and has a significant reduction in cabling compared to the DLR Hand I. As on DLR's Hand I the main goals were to improve autonomous grasping, fine manipulation, as well as power grasp capabilities. A brushed DC motor with a spindle gear is used to relocate the middle and little fingers to help optimize finger placement for specific in-hand tasks. This degree of freedom is limited to unmeasured, slow movement, to reduce weight and complexity of the system.

The actuation system essentially consists of brushless DC–motors, harmonic drive gears, tooth belts and bevel gears in the base joint.

Each joint is equipped with torque sensors based on strain gauges and specially designed potentiometers based on conductive plastic. Besides the torque sensors, a six DOF force torque sensor is placed in the fingertip. The potentiometers are redundant for position measurements, since the joint positions may be calculated from the motor positions. However, they provide the user with more accurate readings of joint positions and can eliminate the necessity of referencing the fingers after power up. In case of not using the potentiometers the elasticity of the transmission belt and the harmonic drive would

have to be considered. With the potentiometer, a resolution of 0.1 degree for the joint angles is achieved.

The hand does not include sensors for velocity but position sensors with high resolution, where the speed can be calculated by differentiation of the position signal. Each motor is equipped with two linear Hall effect sensors. The Hall sensors give just a relative position of the motor and has thus to be referenced after power up.

One major goal of the design of the new DLR Hand was to fully integrate the electronics needed in the fingers and the palm in order to minimize weight, the amount of cables needed for a multi sensory hand, and to increase the reliability by minimizing the amount of cables moved crossing the joints. In case of joints with a single degree of freedom, the problem of reliability was solved by using flexible printed circuit boards with appropriate binding space within the links. Tests showed no visible or measurable effect on the flexible PCB after 100,000 cycles. The power converters for driving the motors are located directly beside the motors and they are galvanically decoupled from the sensor electronics in order to minimize any noise induced by the running motors. Moreover, the different fingers are also galvanically decoupled from each other.

# Chapter 3

# Test setup

## 3.1 Target System

This section presents the five–finger dexterous robot hand DLR/HIT II [34] shown in figure 3.1 which is modelled in this thesis. DLR and HIT (Harbin Institute of Technology) have jointly developed a modular internal actuation DLR–HIT-Hand–I in 2004, the first version of Hand II was finished in 2008.

FIGURE 3.1: DLR-HIT II Hand [35] with modular fingers

The hand has an independent palm and five identical modular fingers, each finger has three DOFs and four joints. All actuators and electronics are integrated in the finger body and the palm. By using flat brushless DC motors (BLDC), tiny harmonic drivers (HD) and smaller electronics, the whole finger's size is about one third smaller than the former finger in the DLR–HIT–Hand–I. At the same time, the multisensory dexterous hand integrates position, force/torque and temperature sensors. The whole weight of the hand is about 1.5 kg and the fingertip force reaches up to 10 N.

On the basis of the DLR–HIT–Hand I, a new super flat BLDC motors design have replaced the traditional BLDC motor format. The motor measures only 20 mm in diameter and 10 mm in height, at a weight of only 15 g. The rated speed and torque of the motor are 6000 rpm and 3.2 mNm respectively. In the finger's distal joint, the mechanical transmission is realized by a timing belt instead of bevel gears, which leads to a noticeably reduced transmission noise. Because of the harmonic drives, the timing belt and the torque sensor joint–flexibility is inherent.

Furthermore two tiny harmonic drives with timing belts have replaced planetary gears and bevel gears at the base joint actuation unit.

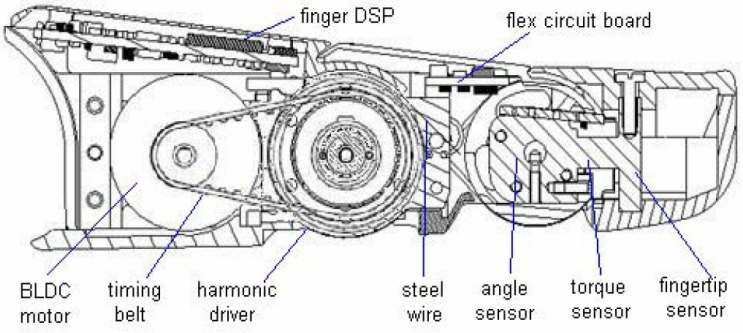


FIGURE 3.2: Finger unit of the DLR/HIT Hand II [34]

One modular finger consists of two independent units: One is the finger body, the other the finger base. In the finger body unit shown in figure 3.2, there is a super flat BLDC motor and a tiny harmonic driver. They are parallelly mounted and transmitted by a high–speed timing belt with a reduction ratio of 1:2.1. The harmonic driver with reduction ratio of 100:1 measures only 20mm in diameter and 13.4mm in length. The maximal driving torque can reach 2.4 Nm. The motions of middle phalanx and distal phalanx are not individually controllable, they are transmitted by means of a steel wire to realize 1:1 coupling movement.

The finger's flexible circuit board is a hard–flexible combination for sensors conditioning and communication, which runs through the rotational joint. This kind of arrangement saves much space because there is no need for any extra electric connectors.

In the finger base unit shown in figure 3.3, the two rotational axes are intersected

For abduction/adduction motion, the motors turn in contrary directions. This causes a curling motion on the fingertip. Using the torque of both motors means reaching double

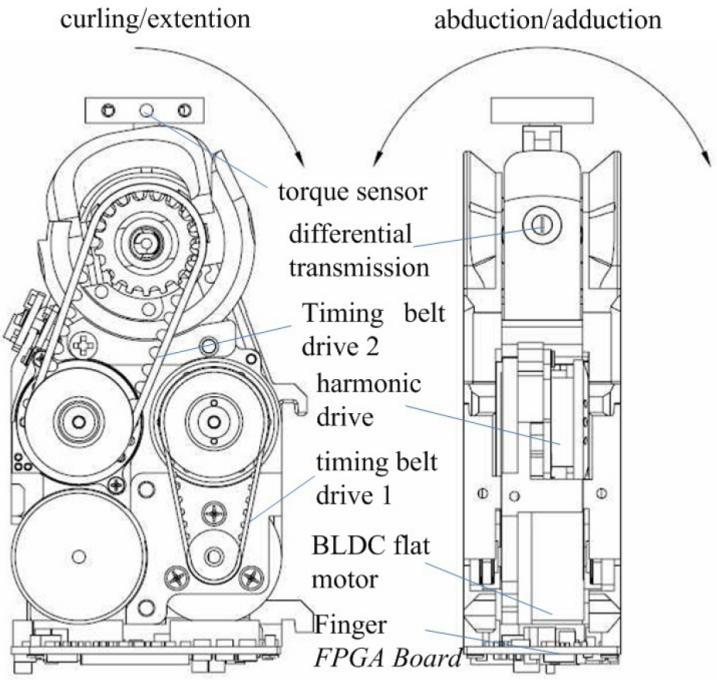


FIGURE 3.3: Finger base joint of the DLR/HIT hand II [34]

output force on the fingertip. Instead of the motor and planetary gear combination in the DLR/HIT Hand I, the finger base actuation uses a system similar to the one in the finger body. Two flat BLDC motors are parallelly placed at the bottom of the base and two harmonic drivers (HD's) are mounted parallelly as well between motors and bevel gears. The transmissions between motor and HD, and between HD and bevel gear are two kinds of timing belts with different strengths. This makes the whole system more consistent and more flexible.

The extra DOF of the thumb in the DLR–HIT–Hand I occured to being not that beneficial to manipulation. Therefore, in the new hand the thumb is fixed in an appropriate orientation of the palm to reduce the number of motors.

Dexterous robot hands need minimum a set of force and position sensors to enable control schemes like position and impedance control in autonomous operation and teleoperation.

The DLR/HIT Hand II has been used for teleoperation in various experiments e. g. [36], [37], [38], [39].

For measuring position, every finger contains potentiometers and Hall sensors. External torques are measured by a new type of proximal joint torque sensor with two DOFs in the fingerbase and another distal torque sensor. Both sensors are based on strain gauges.

In the original hand, each finger was also equipped with a 6–DOF force–torque sensor in the fingertip. However, that the hard surface of the sensor proved to be a limitation for manipulation performance as compared to a compliant rubber fingertip. The 6–DOF force–torque sensor is not currently implemented in the robot finger.

Currently, joint and Cartesian impedance control with friction and gravity compensations is used at the hand. [40]

Cartesian impedance control was first proposed by [9], which established a mass–damper–spring relationship between the Cartesian position $\Delta$x and the Cartesian force F:

$$\mathrm{F} = \mathrm{M}\Delta\ddot{\mathrm{x}} + \mathrm{D}_k\Delta\dot{\mathrm{x}} + \mathrm{K}_k\Delta\mathrm{x} \tag{3.1}$$

where $\mathrm{M}_I$, $\mathrm{D}_k$ and $\mathrm{K}_k$ are positive definite matrices representing the virtual inertia, damping and stiffness of the system [41].

## 3.2 Problem Identification

Not much research is done in the accurate modelling of anthropomorphic hands. Until now, most models of robot hands only include multi body dynamics or friction but not the whole system. [42]

A lot of work is done in modelling robot arms but this often has the goal of suppressing vibration hence modal analysis is used e.g. in [43] or [12]. Hands don't have that much trouble with vibrations so this approach is not beneficial.

Because this model has the goal of enhancing the control performance by including friction, the motor and the manipulator dynamics, many problems have to be taken into account.

- In most models friction is a function of only position and/or velocity but temperature has also significant influence [44].
- The torque of the motor is also temperature dependent.

- At DLR/HIT Hand II, temperature sensors are mounted on the boards but the component which produces most of the heat is the motor, hence the measuring of the motor temperature is not accurate.
- The temperature itself is time dependent as long as the finger is not in a thermodynamic equilibrium.
- Accurate current sensors are big in size and therefore not used in the DLR/HIT Hand II. Furthermore, the embedded motor uses currents in the range of mA thus noise would be an issue.
- Position encoders are expensive. Hence many robot hands as well as DLR/HIT Hand II avoid them.
- Modelling the friction of the harmonic drives requires complex experiments.
- An accurate characterization of the motor is difficult because the produced torques are small and therefore measurements are not precise.

Friction occurs in many components and to model the friction for every component solitary is difficult. A small description about the complexity of modelling the components solitary is given in section 3.2.1 and 3.2.2.

### 3.2.1 Timing belts

Friction in timing belts occurs due to the actual friction between the surfaces of teeth and sprocket and losses through belt noise. The noise is caused by the following effects:

- impact generated by collision of the belt tooth with the bottom land of the sprocket
- collision of the sprocket tooth against the bottom land of the timing belt
- collision of the flanks of the two teeth
- airflow
- frictional noise

[45]. Positioning errors are a result of belt elasticity [46]. Including all these effects would be to complex to pay of.

### 3.2.2 Harmonic Drives

The benefits of Harmonic Drives are no backlash, compactness, light weight and high gear ratios. For these reasons they are often used at the DLR. Harmonic Drives consist of three parts, the wave generator, the circular spline and the flex spline (see figure 3.4).

FIGURE 3.4: Harmonic Drive, left: circular spline, middle: flex spline, right: wave generator [47]

The wave generator is the drive section, whose base body has an elliptical shape and is mounted in a special ball–bearing. Being still flexible, the flex spline has high–strength, torsion proof and external splines. The circular spline is a stiff ring with internal spline and has commonly two teeth more than the flex spline. Inserting the wave generator in the flex spline deforms the flex spline also into an elliptical shape. This combination is inserted into the circular spline. Two contact areas at the long elliptical axis occur, while there is no contact at the short elliptical axis. The rotation of the wave generator results in a rotating deformation of the flex spline, which furthermore leads to rotating contact areas. Because the circular spline has two teeth more than the flex spline this results in a relative motion of flex spline to circular spline. A video with a visual explanation of the functional principle can be found at [48].

Experimental measurements made by Tuttle [49] indicate that friction at non–zero velocities in harmonic drives can be characterized as having three components: velocity–independent friction, velocity–dependent friction and friction from resonant vibration.

According to [50], the best results were seen when the velocity–independent friction was represented by a constant torque value and the velocity–dependent friction torque was approximated by a cubic function of the velocity. Since experimental step–response

data revealed that friction torque could vary substantially with the position of the harmonic–drive output, a sinusoidal friction torque that varied with output rotation was additionally included to capture these effects.

Harmonic drives typically contain kinematic inaccuracies due to manufacturing and assembly errors in the transmission and since these kinematic errors can excite vibrations that influence dynamic performance, they should be recognized in the harmonic drive model. Most friction behaviour is localized at the contact surface between the flex spline and circular–spline wedges.

Since static stiffness measurements are contaminated by transmission and friction, static stiffness tests provided little guidance in this task. Based on this results, it seems unlikely that a modelling, using solely catalogue values or simple experimental observations will be able to make accurate predictions of dynamic performance. Consequently, for applications in which an accurate harmonic drive model is required, there are no short cuts around a detailed experimental analysis of the actual harmonic–drive system.

In particular despite careful measurement and characterization of transmission friction, compliance and kinematic error, model performance could not be improved without acknowledging gear–tooth rubbing losses as well.

To model every element solitary is to complex as written above. Therefore the whole system of transfer elements is considered a “black–box” (called Friction–model 1 - 3 in figure 3.5) with unknown friction behaviour.

Figure 3.5 summarizes the complete model. The motors are controlled via PWM (pulse-width modulation), hence PWM-Signal 1 – 3 is used as input. The motors produce torque, which is transmitted via the transfer elements. Friction occurs at every transfer element but as written above, the friction will be considered as “black–box”. The remaining torque is used to accelerate the finger and therefore used as input for the finger dynamics.

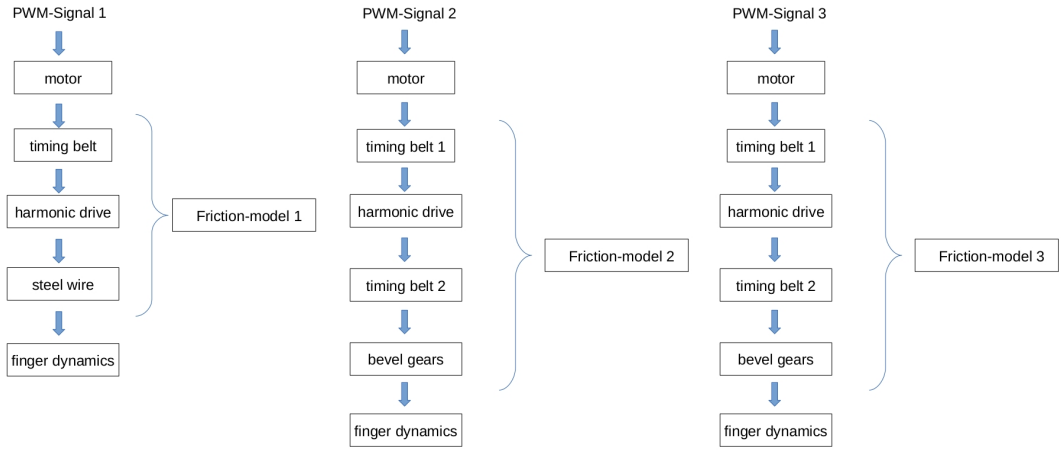


FIGURE 3.5: System of one finger: Friction model 1 combines the friction in the coupled medial and distal joint, Friction model 2 combines the friction in all transfer elements of the first base joint, Friction model 3 combines the Friction in the second base joint.

# Chapter 4

# Manipulator kinematics and dynamics

## 4.1 Introduction

The term end effector ( e.g. a robot hand ) is used to describe the interface between the manipulator (arm) and the environment. The vast majority of end effectors are simple grippers. The goal of this thesis is creating the model of such an end effector for grasping and manipulation. The first part which has to be taken into account is the influence of the dynamics which is outlined below. This requires knowledge about spatial descriptions, manipulator kinematics and dynamics which would be too comprehensive to be fully described in this thesis. For the experienced reader, a small briefing (out of Craig [51]) is included but for readers without knowledge about robot kinematics an appropriate book is recommended. To alleviate this familiarization the same conventions as in Craig are used. Alternatives are e.g. [52] or [53]. For simpler understanding the following notation is used:

- Matrices will be written capitalized and bold.
- Vectors will be written lowercased and bold.
- Skalars will be written normal.

## 4.2 Description of position and orientation

The position and orientation of the end effector, objects that the robot works with and the manipulator itself need to be described for manipulation. To establish these descriptions, coordinate systems and conventions for the relationship between the coordinate systems, positions and orientations are required.

Once an origin coordinate system also referred to as Universe Coordinate System is established, any point can be located with a $3 \times 1$ position vector. For manipulator dynamics, the definition of many coordinate system is often necessary, as a result vectors have to be referenced to a specific coordinate system. This is achieved by a leading superscript. For example: ${}^{A}\mathbf{p} = (\mathrm{p}_x\ \mathrm{p}_y\ \mathrm{p}_z)^T$
Vector $\mathbf{p}$ is referring to coordinate system A.

To describe the orientation, a coordinate system is attached to the body. In order to specify the orientation of the attached coordinate system to another coordinate system, a rotation matrix is used. ${}^{A}_{B}\mathbf{R}$ specifies the rotation of coordinate system B relative to A.

With an appropriate positioning of the coordinate systems, the calculations for an end effector can be simplified to rotations around the principle axes of the particular coordinate system.

If a rotation is described by three $3 \times 1$ vectors nine parameters are required. On the other hand, the concept of Eulers Angles needs just three parameters. Every orientation can be achieved by rotating one time around every principle axis. These three angles are used as parameters for the Euler Angles instead of three vectors.

The rotation around the principle axes is defined as follows:

$$\mathbf{R}_x(\alpha) = \begin{bmatrix} 1 & 0 & 0 \\ 0 & cos\alpha & -sin\alpha \\ 0 & sin\alpha & cos\alpha \end{bmatrix} \tag{4.1}$$

$$\mathbf{R}_y(\alpha) = \begin{bmatrix} cos\alpha & 0 & sin\alpha \\ 0 & 1 & 0 \\ -sin\alpha & 0 & cos\alpha \end{bmatrix} \tag{4.2}$$

$$\mathbf{R}_z(\alpha) = \begin{bmatrix} 0 & cos\alpha & -sin\alpha \\ 0 & sin\alpha & cos\alpha \\ 0 & 0 & 1 \end{bmatrix} \tag{4.3}$$

From linear algebra, it is known that the inverse of a rotation matrix is equal to its transpose.

$${}^A_B\mathbf{R} = {}^B_A\mathbf{R}^{-1} = {}^B_A\mathbf{R}^T \tag{4.4}$$

The situation of a position and an orientation pair arises so often in robotics, that an entity called frame is defined which is the combination of a rotation matrix and a position vector to the origin of this matrix respectively the attached coordinate system.

To change the position of a point a vector is required. To change the orientation of a point a rotation matrix is used. To combine these two a new operation is introduced, the so called transformation matrix.

$${}^A\mathbf{p} = {}^A_B\mathbf{R}{}^B\mathrm{P} + {}^A\mathbf{p}_{BORG} \tag{4.5}$$

With ${}^A\mathbf{p}_{BORG}$ is a vector to the origin of coordinate system B.

$${}^A\mathbf{p} = {}^A_B\mathbf{T}{}^B\mathbf{p} \tag{4.6}$$

$$\begin{bmatrix} {}^A\mathbf{p} \\ 1 \end{bmatrix} = \begin{bmatrix} {}^A_B\mathbf{R} & {}^A\mathbf{p}_{BORG} \\ 0\ 0\ 0 & 1 \end{bmatrix} \begin{bmatrix} {}^B\mathbf{p} \\ 1 \end{bmatrix} \tag{4.7}$$

Just as a rotation matrix specifies an orientation, using transformation matrices specifies a frame.

## 4.3 Kinematics

Once the position and orientation are described, the next step is to describe the motion. Kinematics is the branch of classical mechanics which describes the motion without taking into consideration the required forces that cause them. In order to deal with the complex geometry of a manipulator, frames are fixed to various parts of the mechanism and the relationships between these frames are described. The study of manipulator kinematics involves, among other things, how the locations of these frames change as the mechanism actuates. The central topic of this section is a method to compute the position and orientation of the manipulator's end effector relative to the base of the manipulator as a function of the joint variables.

### 4.3.1 Link description

Most mechatronic systems consists of a set of bodies connected to each other by joints. These bodies are called Links. Typical joints are classified into cylindrical, planar, screw, spherical, prismatic and revolute joints. The most common two joints are revolute and prismatic. The links are numbered starting from the immobile base, which is mostly called link 0. The first moving link is link 1, and so on. The length of a link is the shortest distance between the axes of the joints of the link.

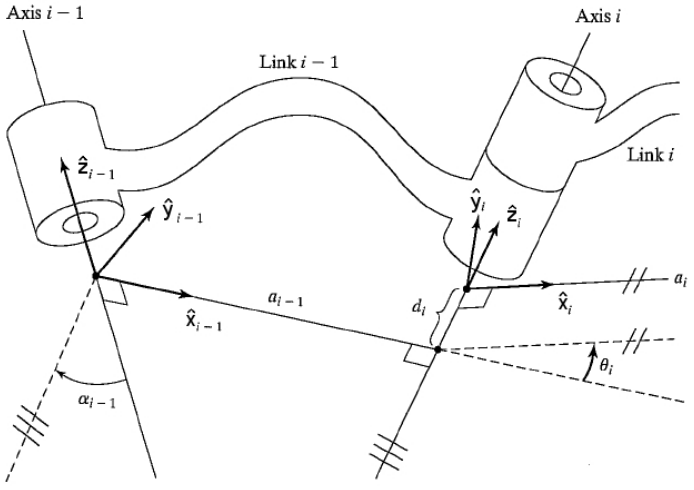


FIGURE 4.1: Link–description adjusted version of [51] page 68: $d_i$ = link offset, $\theta_i$ = joint angle, $a_i$ = link length, $\alpha_i$ = link twist

With four values for each link any manipulator can be described kinematically, two for the link itself and two for the link's connection to the neighbouring links. Describing links with these quantities is called the Denavit–Hartenberg notation. In the case of revolute joints link offset, link length and link twist are fixed values and the joint angle is the variable specifying the kinematics of the manipulator.

To describe the location of each link a frame is attached to each link. These frames are numbered according to the attached link. The orientation and placement of the frame is as follows: $\hat{\mathbf{z}}_i$ = axis of joint$_i$ and $\hat{\mathbf{x}}_i$ = axis of link length in the direction of Link$_{i+1}$.

| i | $\alpha_{i-1}$ | $a_{i-1}$ | $d_i$ | $\theta_i$ |
|---|---|---|---|---|
| 1 | 90° | $L_0$ | 0 | $\theta_1$ |
| 2 | 0° | $L_1$ | 0 | $\theta_2$ |
| 3 | 0° | $L_2$ | 0 | $\theta_3$ |
| 4 | 0° | $L_3$ | 0 | $\theta_4$ |

TABLE 4.1: Link parameter of the four–link–manipulator in figure 4.2

As written in section 3.1 the DLR/HIT Hand II uses a bevel gear mechanism in the finger base to achieve two DOF and two revolute joints for the proximal and distal joint. To model the two DOF of the bevel gear mechanism with revolute joints, the joints around $\theta_1$ and $\theta_2$ in figure 4.2 are rotated around $\mathbf{x}_1$ of 90° and the length of $L_0$ is set to zero. Rotation of the proximal and distal joint is represented by deriving $\theta_3$ and $\theta_4$.

### 4.3.2 Joint space and Cartesian space

The position of all links of a N–DOF–manipulator is specified with N joint variables. This set is often referred to as the N × 1 joint vector. The space which these joint vectors create is called joint space. Knowing the joint space description the cartesian space is calculated with the above described kinematics. Synonyms for the cartesian space are task orientated space or operational space.

### 4.3.3 Velocities and static forces

As described in the introduction, the function of an end effector is to grasp and manipulate objects. One finger of the DLR/HIT Hand II is described as a 4 link manipulator. The position can be described via the four angles $\theta_1, \theta_2, \theta_3, \theta_4$. Thus the next step is

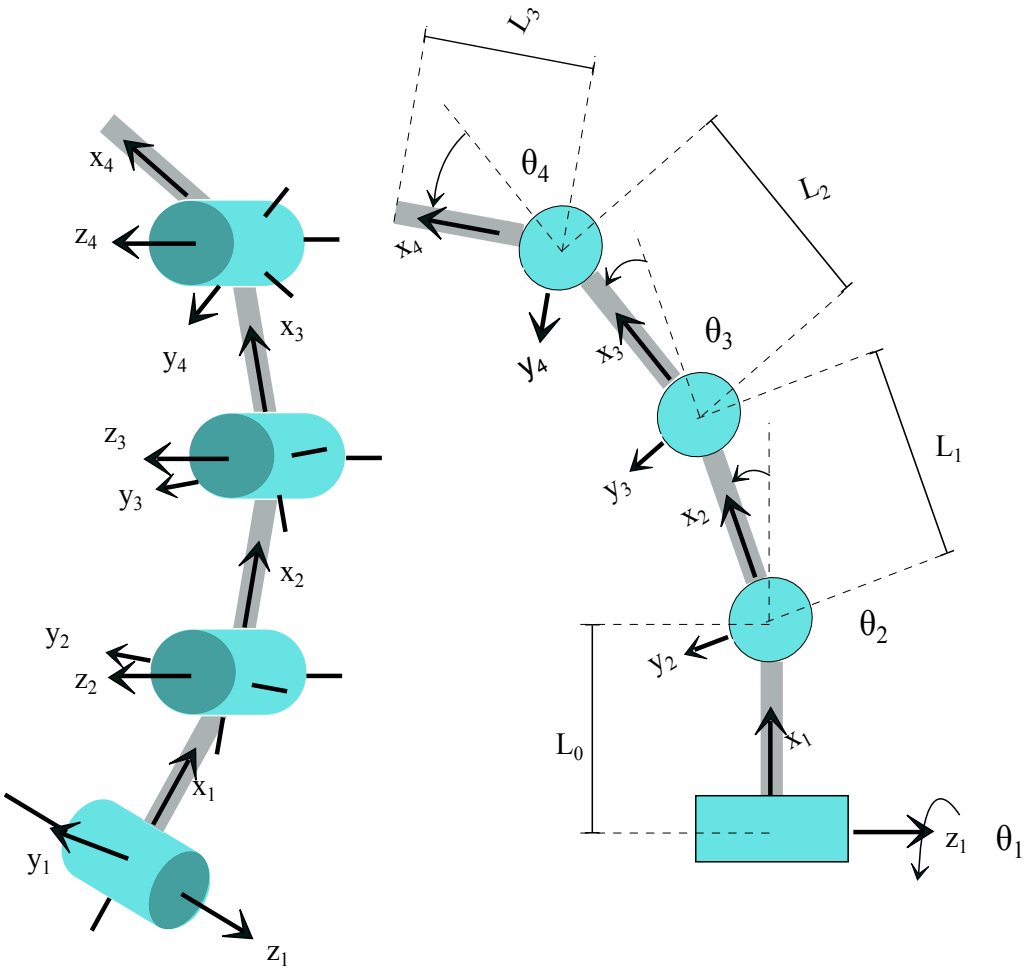


FIGURE 4.2: Four–link–manipulator to model one finger of DLR/HIT Hand II

to expand the considerations beyond static positioning problems to motion and static forces.

Linear velocity will be written as $\mathbf{v}$. For example, ${}^{B}\mathbf{v}_{Q}$ describes the velocity of the point Q in terms of the coordinate system A. Rotational respectively angular velocity will be written as $\dot{\theta}\hat{\mathbf{z}} = \omega$. Every manipulator consists of a chain of bodies which are capable of motion. In order to calculate the velocities, the velocity of each link is calculated and added starting from the base. To add rotational velocities both $\omega$ vectors have to be written with respect to the same frame. The angular velocity of link $i+1$ is the same as that of link i plus the caused component of joint $i+1$.

## 4.4 Manipulator dynamics

The reason to calculate the manipulator dynamics is to find the forces required to cause motion. Referred to the robot finger, the goal is to find the dependence between the applied torques and the resulting movements of the finger. The two common approaches are the Lagrangian formulation of manipulator dynamics or the iterative Newton – Euler dynamic formulation. While the Newton – Euler approach is "force balance" the Lagrangian formulation is an "energy–based" approach. Due to the simpler and more effective implementation of the Newton – Euler approach in Matlab, especially with increasing number of links, this approach was chosen.

The algorithm for computing joint torques composes of two parts. First of all, rotational velocities and linear accelerations of every center of mass need to be calculated in order to get the resulting forces and torques. The second part is to calculate the influence of interacting forces and to sum both terms to calculate the required torques.

Outward iterations: i: $0 \rightarrow 5$

$$ {}^{i+1}\boldsymbol{\omega}_{i+1} = {}^{i+1}_{i}\mathbf{R}\,{}^{i}\boldsymbol{\omega}_{i} + \dot{\theta}_{i+1}\,{}^{i+1}\hat{\mathbf{z}}_{i+1} \tag{4.8} $$

$$ {}^{i+1}\dot{\boldsymbol{\omega}}_{i+1} = {}^{i+1}_{i}\mathbf{R}\,{}^{i}\dot{\boldsymbol{\omega}}_{i} + {}^{i+1}_{i}\mathbf{R}\,{}^{i}\boldsymbol{\omega}_{i} \times \dot{\theta}_{i+1}\,{}^{i+1}\hat{\mathbf{z}}_{i+1} + \ddot{\theta}_{i+1}\,{}^{i+1}\hat{\mathbf{z}}_{i+1} \tag{4.9} $$

$$ {}^{i+1}\dot{\mathbf{v}}_{i+1} = {}^{i+1}_{i}\mathbf{R}({}^{i}\dot{\boldsymbol{\omega}}_{i} \times {}^{i}\mathbf{p}_{i} + {}^{i}\boldsymbol{\omega}_{i} \times ({}^{i}\boldsymbol{\omega}_{i} \times {}^{i}\mathbf{p}_{i+1}) + {}^{i}\dot{\mathbf{v}}_{i}) \tag{4.10} $$

$$ {}^{i+1}\dot{\mathbf{v}}_{C_{i+1}} = {}^{i+1}\dot{\boldsymbol{\omega}}_{i+1} \times {}^{i+1}\mathbf{p}_{C_{i+1}} + {}^{i+1}\boldsymbol{\omega}_{i+1} \times ({}^{i+1}\boldsymbol{\omega}_{i+1} \times {}^{i+1}\mathbf{p}_{C_{i+1}}) + {}^{i+1}\dot{\mathbf{v}}_{i+1} \tag{4.11} $$

$$ {}^{i+1}\mathbf{F}_{i+1} = m_{i+1}\,{}^{i+1}\dot{\mathbf{v}}_{C_{i+1}} \tag{4.12} $$

$$ {}^{i+1}\mathbf{N}_{i+1} = {}^{C_{i+1}}\mathbf{I}_{i+1}\,{}^{i+1}\dot{\boldsymbol{\omega}}_{i+1} + {}^{i+1}\boldsymbol{\omega}_{i+1} \times {}^{C_{i+1}}\mathbf{I}_{i+1}\,{}^{i+1}\boldsymbol{\omega}_{i+1} \tag{4.13} $$

Inward iterations: i: $6 \rightarrow 1$

$$ {}^{i}\mathbf{f}_{i} = {}^{i}_{i+1}\mathbf{R}\,{}^{i+1}\mathbf{f}_{i+1} + {}^{i}\mathbf{F}_{i} \tag{4.14} $$

$$ {}^{i}\mathbf{n}_{i} = {}^{i}\mathbf{N}_{i} + {}^{i}_{i+1}\mathbf{R}\,{}^{i+1}\mathbf{n}_{i+1} + {}^{i}\mathbf{p}_{C_i} \times {}^{i}\mathbf{F}_{i} + {}^{i}\mathbf{p}_{i+1} \times {}^{i}_{i+1}\mathbf{R}\,{}^{i+1}\mathbf{f}_{i+1} \tag{4.15} $$

$$ \tau_{i} = {}^{i}\mathbf{n}_{i}^{T}\,{}^{i}\hat{\mathbf{z}}_{i} \tag{4.16} $$

The effect of gravity loading on the links can be included quite simply by setting ${}^0\dot{\mathbf{v}}_0 = \mathbf{g}$, where $\mathbf{g}$ has the magnitude of the gravity vector but points in the opposite direction. This is equivalent to saying that the base of the robot is accelerating upward with 1 g acceleration.

## 4.5 Resulting m–file

The iterative – Newton – Euler formalism was implemented into Matlab shown in Appendix A, which yields the formulas for the torque of a 4–link manipulator. In order to get the dynamics of a finger, some parameters have to be changed. The first two joints are actually at the same position of the finger base. Hence $l_0$ has to be set to zero. The last two joints are coupled via a steel wire, so $\theta_4 = \theta_3$ as well as their derivatives are equal. Also the torque calculated for joint 4 has to be added to joint 3. The equations for the three torques have the form of equation 4.17.

$$\boldsymbol{\tau} = \mathbf{M}(\theta, \ddot{\theta}) + \mathbf{C}(\theta, \dot{\theta}) + \mathbf{G}(\theta) \tag{4.17}$$

For easier handling the Matlab script separates the three terms. The next step consists on solving the equation for acceleration. For that purpose, the mass term has to be separated into the form $\mathrm{M\_}i(\theta)\ddot{\theta}_i + \mathrm{M\_rest\_i}(\theta, \ddot{\theta})$.

The term $\mathrm{M\_rest\_i}(\theta, \ddot{\theta})$ represents resulting forces through the acceleration of the other joints while $\mathrm{M\_}i(\theta)$ represents the inertia for accelerations around joint i. Therefore the Matlab script separates the mass term for each joint in M_i and M_rest_i. This yields to the following formulas:

$$\tau_1 = \mathrm{M\_1} \cdot \ddot{\theta}_1 + \mathrm{M\_1\_}rest + \mathrm{C\_1} + \mathrm{G\_1} \tag{4.18}$$

$$\tau_2 = \mathrm{M\_2} \cdot \ddot{\theta}_2 + \mathrm{M\_2\_}rest + \mathrm{C\_2} + \mathrm{G\_2} \tag{4.19}$$

$$\tau_3 = \mathrm{M\_1} \cdot \ddot{\theta}_3 + \mathrm{M\_3\_}rest + \mathrm{C\_3} + \mathrm{G\_3} \tag{4.20}$$

Equations 4.18 – 4.20 express the torque at the actuators as functions of joint position, angular velocity and acceleration. The calculated terms for M_i, M_i_rest, C_i and G_i are shown in Appendix B. For simulating the manipulator, these equations have to be solved for acceleration.

$$\ddot{\theta}_i = \frac{\tau_i - \text{M\_i\_rest} - \text{C\_i} - \text{G\_i}}{\text{M\_i}} \tag{4.21}$$

# Chapter 5

# Modelling the Motor

## 5.1 Goal of the modeling

As described in the previous chapter, the mass term, the centrifugal term and gravitational term are already determined. The next step is to characterize the motor torque $\tau_i$ of equation 4.21.

## 5.2 Basics about the motor

As the name implies, the BLDC motors do not use brushes for commutation, instead, they are electronically commutated. The BLDC motors have many advantages over brushed DC motors and induction motors, for example:

- Better speed versus torque characteristics
- High dynamic response
- High efficiency
- Long operating life
- Noiseless operation
- Higher speed ranges

In addition, the ratio of torque delivered to the size of the motor is higher. [54]

The motor converts electrical power $P_{el}$ in mechanical power $P_{mech}$. Power loss occurs through friction $P_F$ and heat loss $P_J$. This yields to the following equations:

$$\mathrm{P}_{el} = \mathrm{P}_{mech} + \mathrm{P}_J + \mathrm{P}_F \tag{5.1}$$

$$\mathrm{P}_{el} = \mathrm{U} \cdot \mathrm{I} \tag{5.2}$$

U: voltage

I: current

$$\mathrm{P}_{mech} = \frac{\pi}{30000} \tau \cdot \mathrm{n} \tag{5.3}$$

$\tau$: torque

n: rotational speed

$$\mathrm{P}_J = \mathrm{R(T)} \cdot \mathrm{I}^2 \tag{5.4}$$

$R(T)$: temperature dependent resistance

A higher temperature influences the resistance of the coils R(t) which is responsible for the heat loss.

$$\mathrm{R(T)} = \mathrm{R}_0 \cdot (1 + \alpha_T(\mathrm{T} - \mathrm{T}_0)) \tag{5.5}$$

T: temperature

$\mathrm{T}_0$: surrounding temperature

$\alpha_T$: temperature coefficient

$\mathrm{R}_0$: Resistance of the coil at surrounding temperature

$$U \cdot I = \frac{\pi}{30000}\tau \cdot n + R(T) \cdot I^2 + P_F \tag{5.6}$$

For the example of copper coils, increasing the temperature by 50 K increases the resistance by about 20 %. [55] In the matter of motor control for the DLR/HIT Hand II Pulse–width modulation (PWM) is used to adjust the required motor torque. The PWM signal can be set from 0 (no voltage) to 4096 (continuous voltage).

## 5.3 Test setup

To characterize the motor the test bed shown in figure 5.1 was built.

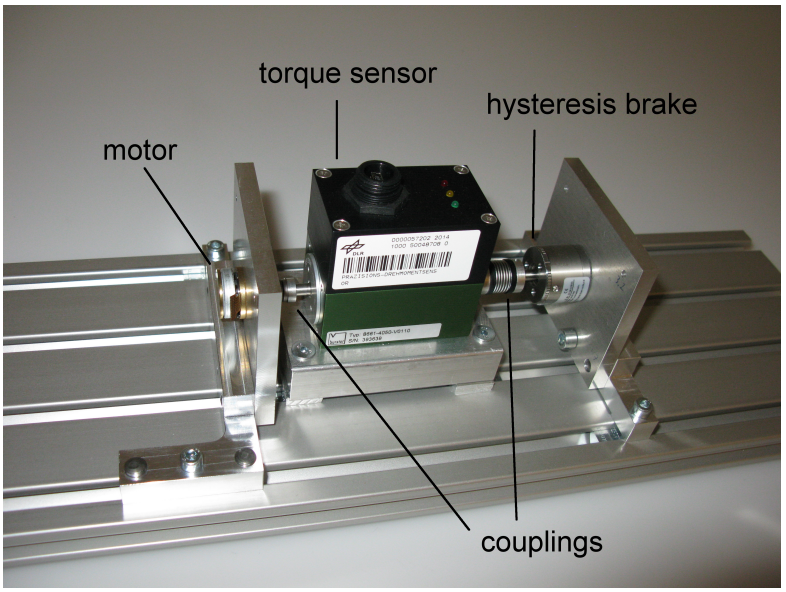


FIGURE 5.1: Test bed for torque measurements. Maxon EC 20 flat motor on the left, Burster 8661 torque sensor in the middle, mobac 513 hysteresis brake on the right, connected via steel bellow couplings

The test bed consists of four different components. On the left side is one of the maxon motors currently used in the DLR/HIT hand II with a maximum continuous torque of 3.2 mNm [56]. In the middle a Burster 8661 torque sensor with a measurement range of $\pm$ 5 Ncm [57] is used. The sensor has an accuracy of $\leq \pm$ 0.05 % F.S.. The measurement inaccuracy is therefore $\pm$0.005 Ncm On the right a 513 hysteresis brake from Mobac [58] is placed. The benefits of hysteresis brakes are a velocity independent force, high lifespan and a smooth torque.

To compensate alignment errors due to manufacturing inaccuracies the three components are connected with steel bellows couplings. The mechanism is mounted on a item profile plate. The motor is controlled by the controller of the hand and the output of the sensor is saved with the provided software DigiVision.

## 5.4 Dataresults

The first measurement was a sweep over different PWM signals, as shown in figure 5.2. The PWM signal was increased with a step function from 0 (no signal) to 4000 ($\frac{4000}{4096} \times 100$ % of continuous voltage) in steps of 50 every 10 seconds. Between every step the PWM signal was set to zero for 10 seconds.

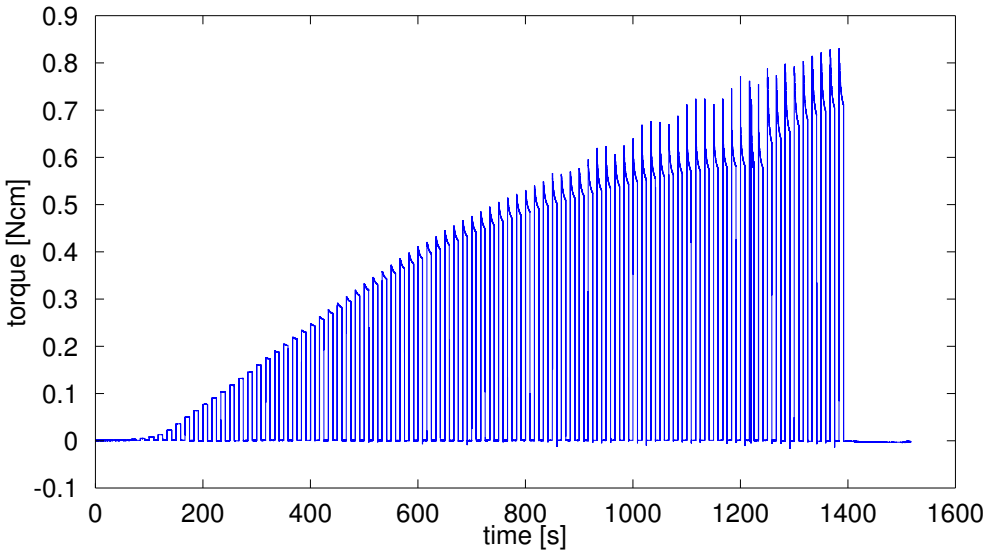


FIGURE 5.2: PWM sweep over the full range, for small PWM signals constant torque, higher PWM signals result in a time dependent torque due to heating up

Based on figure 5.2, it is shown, that the torque increases with the increasing PWM signal. For the first signals, the torque has a rectangular shape but for higher PWM signals, the torque is falling over time. Given that the motor heats up more with higher power inputs and the resistance of the coils therefore rises (shown in equation 5.4) it is verified, that the torque is also temperature dependent. According to equation 5.3 the torque depends also on the velocity.

In summary, the torque is a function of PWM signal, rotational speed and temperature which is time dependent if the motor is not in a thermodynamic equilibrium, which can

be described as $\tau$(PWM, $\omega$, T(t)). In order to characterize the torque two of the three parameters were hold constant while varying the other parameter.

### 5.4.1 Torque - PWM - relation

To figure out the relationship between the PWM signal and the torque the other parameters have to be neglected. To do so, the force of the brake was set to the maximum (14 mNm) to achieve a velocity of zero for each measurement. This also has the positive effect of minimizing measurement errors due to misalignments in the test bed.

Additionally, a heat up phase was implemented before measuring the torque to maintain a defined temperature shown in figure 5.3. For this heat up phase a PWM signal of 3000 was set for 250 seconds. This PWM signal is approximately the average PWM signal in operation and therefore represents the operating temperature.

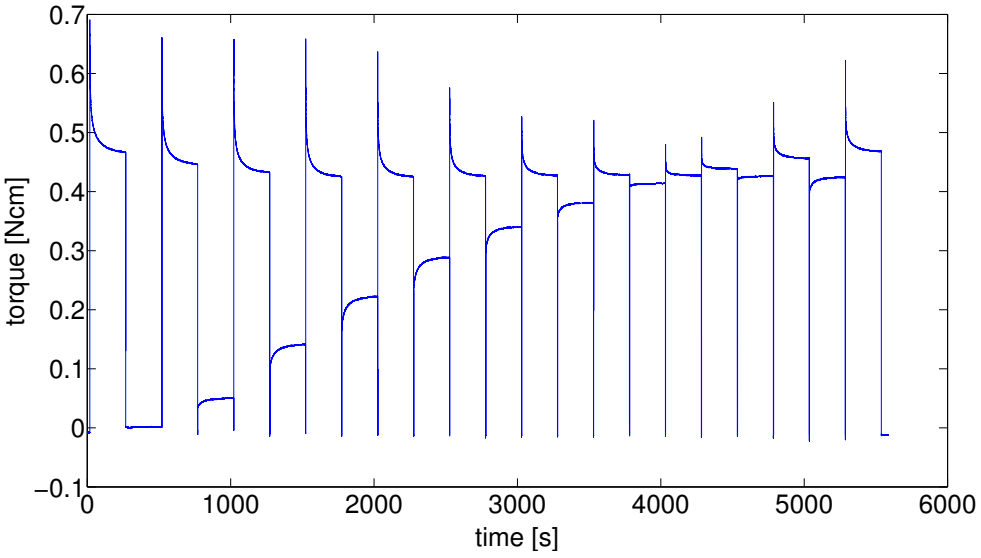


FIGURE 5.3: PWM sweep with heat up phase to compensate temperature influence and no velocity to neglect velocity dependence

Because this measurement was taken under room temperature only the first few measurement values after the heat up phases have a similar temperature due to thermodynamic balancing processes and can be taken into account. For PWM signals smaller than the PWM signal used in the heat up phase the temperature is falling over time, therefore the torque increases over time. On the other hand, PWM signals which are bigger than the heat up signal, result in a decreasing torque over time.

This leads to the following relationship of torque to PWM signal as shown in figure 5.4.

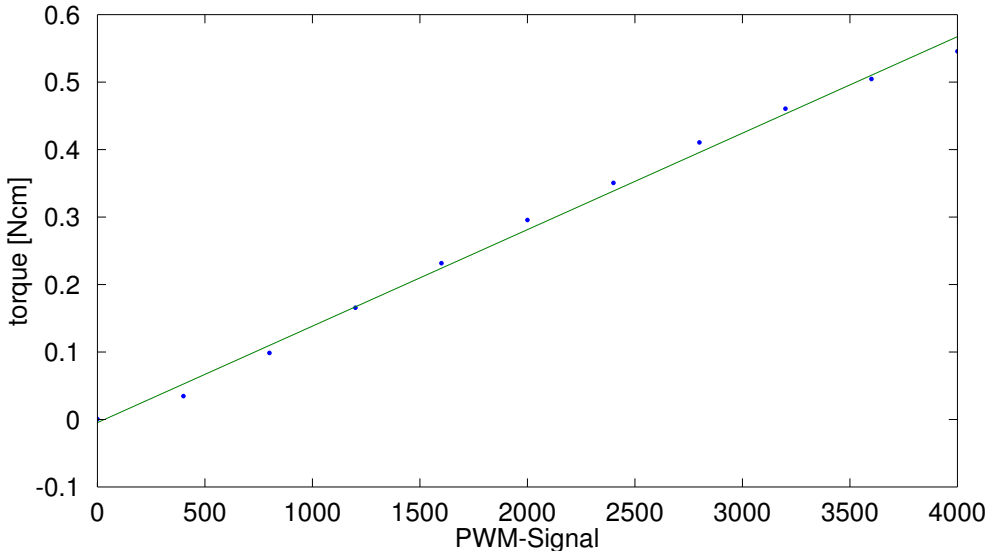


FIGURE 5.4: Torque/PWM signal relation approximated with linear function

The measurement of figure 5.4 slightly shows the behaviour of a third degree polynomial but since the aberration of a straight line is so small the measured values are approximated as the linear function in equation 5.7.

$$\tau = 1.43 \cdot 10^{-4} \frac{\text{Ncm}}{\text{PWM}} \cdot \text{PWM} \tag{5.7}$$

### 5.4.2 Torque - velocity - relation

To figure out the relationship between rotational speed and torque, it is required to hold the temperature and PWM signal constant. Luckily the biggest influence for temperature is the produced heat due to the current. Hence a constant PWM signal yields nearly a constant temperature. As shown in figure 5.5 (a), the speed was changed in steps of around 500 rpm (rotations per minute) from zero to 2500. Due to the fact, that the brake allows only to change the applied torque, changing the velocity had been done manually.

Huge noise can be observed in figure 5.5 (b). It is assumed that the changing torque is a result of misalignment of the axis of motor, sensor and brake which leads to an oscillating torque. To calculate the torque used in figure 5.6, the arithmetic mean over a few thousand measurement values was built.

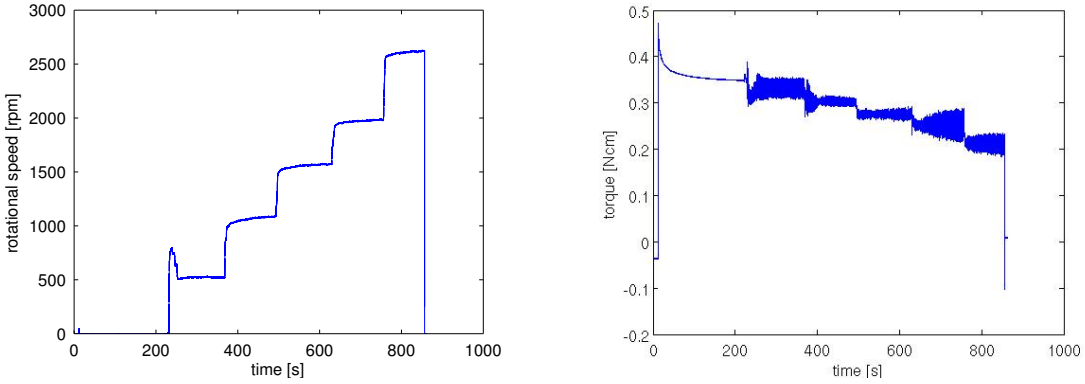


FIGURE 5.5: Speed over time (a), Torque over time (b) the velocity was set manually, the huge noise in (b) is assumed to be a result of misalignment on the test bed

This measurement was repeated for PWM signals of 2000, 2500, 3000, 3500 and 4000. The results are shown in figure 5.6.

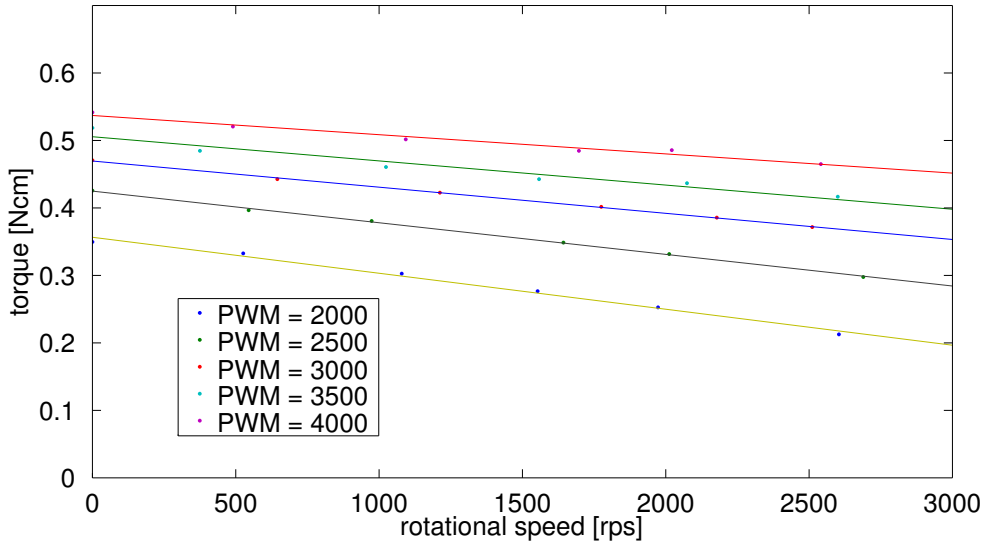


FIGURE 5.6: Torque over speed for different PWM signals, for every PWM signal a linear relationship between torque and velocity is assumed, the slope depends on the PWM signal

The relationship between rotational speed and torque is also approximated via a linear function. The calculated functions are:

$$\Delta\tau_i = b(\text{PWM}) \cdot \omega$$

$$\Delta\tau_{2000} = -5.332 \cdot 10^{-5} \cdot \omega$$

$$\Delta\tau_{2500} = -4.688 \cdot 10^{-5} \cdot \omega$$

$$\Delta\tau_{3000} = -3.876 \cdot 10^{-5} \cdot \omega$$

$$\Delta\tau_{3500} = -3.582 \cdot 10^{-5} \cdot \omega$$

$$\Delta\tau_{4000} = -2.847 \cdot 10^{-5} \cdot \omega$$

To estimate if it is beneficial to include the different slopes or use the average it was argued as followed. The highest speed the finger achieves are about 250 $^\circ/s$. Multiplied by 100 for the transmission ratio of the HD and 2.1 for the belt, the motor rotates with a velocity of 42,000 °/s = 117 rps = 7000 rpm. The average of the slopes is $-4.065 \cdot 10^{-5} \frac{\text{Ncm}}{\text{rpm}}$.

So the error for a PWM signal of 2000 and 4000 using the average is:

$$(-5.332 \cdot 10^{-5} \tfrac{\text{Ncm}}{\text{rpm}} - -4.065 \tfrac{\text{Ncm}}{\text{rpm}}) \cdot 7000\text{rpm} = -0.089 \text{ Ncm}$$
$$(-2.847 \cdot 10^{-5} \tfrac{\text{Ncm}}{\text{rpm}} - -4.065 \tfrac{\text{Ncm}}{\text{rpm}}) \cdot 7000\text{rpm} = +0.085 \text{ Ncm}$$

With a nominal torque of 0.32 Ncm the error is bigger than 25 % hence a discrimination between the different slopes has to be done. This dependency is approximated via
$\text{b} = 1.215 \cdot 10^{-8} \frac{\text{Ncm}}{\text{rpm} \cdot \text{PWM}} \cdot \text{PWM} - 7.711 \cdot 10^{-5} \frac{\text{Ncm}}{\text{rpm}}$

$$\Delta\tau = \text{b(PWM)} \frac{\text{Ncm}}{\text{rps}} \cdot \omega \tag{5.8}$$

where $\omega$ represents rotational speed.

### 5.4.3 Influence of Temperature

The influence of temperature is one of the bigger problems in modelling the motor. In the worst case shown in figure 5.7, a PWM signal of 4000 leads to a torque of nearly 1 Ncm at room temperature and a velocity of zero but over time the motor temperature reaches about 80° C which results in a torque of less then 0.6 Ncm. In the DLR/HIT Hand II, the temperature sensors are mounted on FPGA boards and the distance to the motor makes it impossible to measure the motor temperature. Hence the model has to assume a temperature. Therefore the heat up phase in figure 5.4.1 was set to PWM = 3000 and it was stated that the hand has to be in operation for a few minutes to get the proper operating temperature for using the motor model.

## 5.5 Conclusion

This leads to the following formula

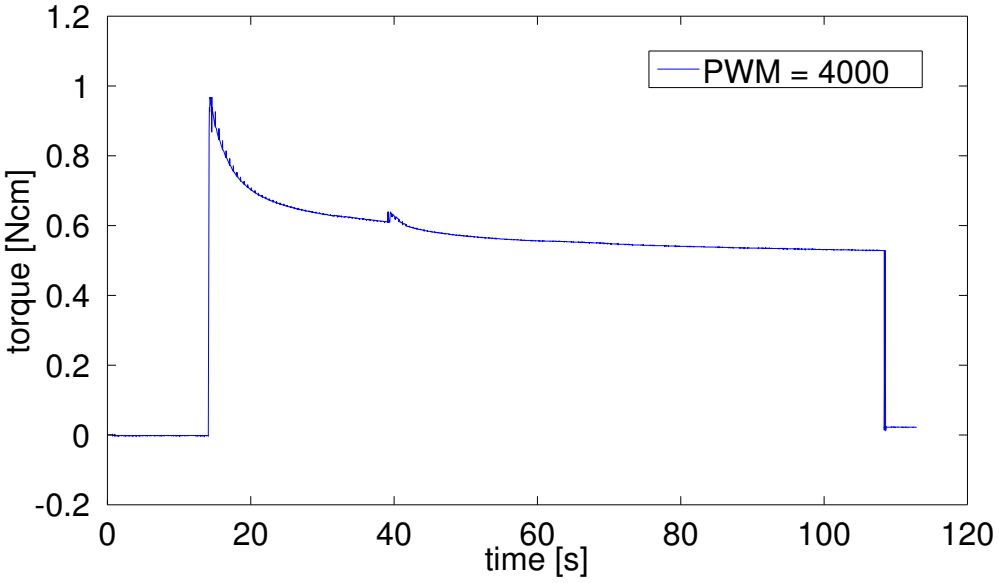


FIGURE 5.7: Temperature–Sweep

$$\tau(\mathrm{PWM}, \omega, \mathrm{T}) = ((\mathrm{a} \cdot \mathrm{PWM}) + (\mathrm{b}(\mathrm{PWM}) \cdot \omega)) \cdot (1 - \alpha_{Copper}(\mathrm{T} - \mathrm{T}_0)) \tag{5.9}$$

Neglecting the temperature and using the parameter from equation 5.7 and 5.8 leads to:

$$\begin{aligned} \tau(PWM, \omega) =& (1.43 \cdot 10^{-4} \frac{\mathrm{Ncm}}{\mathrm{PWM}} \cdot \mathrm{PWM}) \\ &+ (1.215 \cdot 10^{-8} \frac{\mathrm{Ncm}}{\mathrm{rpm} \cdot \mathrm{PWM}} \cdot \mathrm{PWM} - 7.711 \cdot 10^{-5} \frac{\mathrm{Ncm}}{\mathrm{rpm}}) \cdot \omega \end{aligned} \tag{5.10}$$

# Chapter 6

# Modelling the friction

## 6.1 Friction Introduction

Friction occurs in most moving systems and is the reason for significant control errors and undesired stick–slip–movements. Depending on the rank of non–linearity, it is often only possible to compensate the friction near to a operating point with classic linear control–concepts. By using air or magnetic bearings, mechanical friction can mostly be neglected, but on the contrary aerodynamic or magnetic effects occur which are also difficult to address. [59]

The easiest way to describe friction between two surfaces is using the Coulomb–model equation 6.1. The main idea is that friction opposes motion and that its magnitude is independent of velocity and contact area.

$$\mathrm{F}_c = \mathrm{F}_N \cdot \mu \tag{6.1}$$

Multiplying the Coulomb friction with the signum Function, leads to an opposing force independent of the direction of the motion shown in equation 6.2.

$$\mathrm{F} = sign(\omega)\mathrm{F}_c \tag{6.2}$$

Viscous friction is caused by the viscosity of lubricants, therefore a viscous term is added in equation 6.3.

$$\mathrm{F} = sign(\omega)(\mathrm{F}_c + \sigma\omega) \tag{6.3}$$

Where $\sigma$ is the viscous coefficient of the lubricant.

This model is used often in robotics, for example for the Robonaut2 [60].

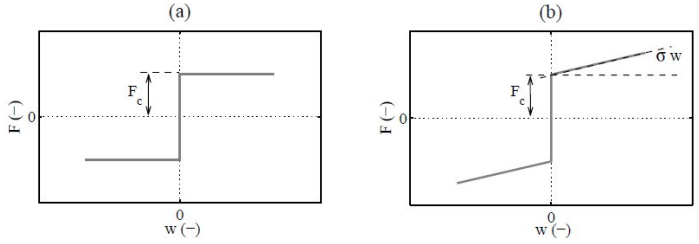


FIGURE 6.1: Coulomb friction (a) and viscous friction (b) [59]

Time dependent conditions like temperature cause additional uncertainties. For example depending on the temperature the viscosity of the lubricant changes. Although a temperature dependent model of the friction seems reasonable mostly temperature is not taken into account. The thermodynamic behaviour is often to complex for a workable model, additionally, it is difficult to measure the exact temperature at the contact surfaces. Besides the dry and viscous kinetic friction, where the velocity is assumed to be $\omega \neq 0$, the kinetic friction is also influenced by the static friction. The static friction (stiction) specifies the maximum break–away–force right before the resting body starts moving. Hence, the static friction is not a function of velocity, but depends on the normal force and the properties of the two surfaces.

Stiction is short for static friction as opposed to dynamic friction. It describes the friction force at rest. Stiction counteracts external forces below a certain level and thus keeps an object from moving. It is clear that stiction can not be described as a function of only velocity. Instead it has to be modelled using the external force. The stiction a function of the external force and not the velocity.

Analog to the coulomb friction, the stiction is defined as:

$$\mathrm{F}_s \leq \mu_h \mathrm{F}_N \tag{6.4}$$

The crossover between stiction and dynamic friction is described by the Stribeck–Effect [61]. The Stribeck–Curves are shown in figure 6.2

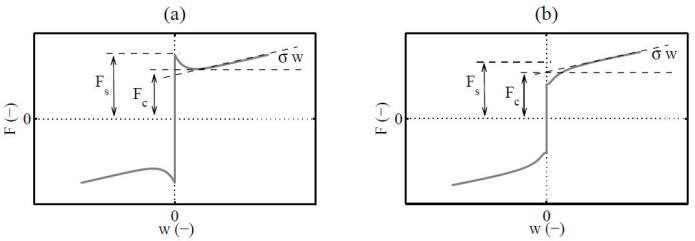


FIGURE 6.2: Stribeck–friction with positive shape–factor (a) and negative shape–factor (b) [59]

The commonly used formula for the Stribeck–Effect is:

$$sgn(\omega)(\mathrm{F}_c + (\mathrm{F}_s - \mathrm{F}_c) \cdot exp(-|\frac{\omega}{\mathrm{V}_s}^{\delta}|)) + \sigma\omega \tag{6.5}$$

Where $V_s$ is the so called Stribeck–velocity and $\delta$ the Stribeck–shape–factor.

## 6.2 Parameter estimation

Models like the Stribeck model assume that friction is only a function of velocity. As written in section 3.2.2, the friction of harmonic drives is also position dependent. Including the friction $F(\theta, \dot{\theta})$ the dynamic equation looks like:

$$\ddot{\theta}_i = \frac{\tau_i - \mathrm{M\_}i\_rest - \mathrm{C\_}i - \mathrm{G\_}i - \mathrm{F}_F(\theta, \dot{\theta})}{\mathrm{M\_}i} \tag{6.6}$$

We are able to measure the position with the hall sensors integrated in the hand and derive the velocity. To derive a second time, to get the acceleration is not precise and therefore neglected.

Thus a torque is applied, when the velocity is nearly constant (acceleration = 0) (e.g. in the area next to the operating point in figure 6.3) the term $\mathbf{M}(\theta)\ddot{\theta}$ can be neglected.

$\tau$ is modelled as a function of the PWM signal and velocity see Chapter 4.

Finally, the equation can be solved for friction.

| PWM | Position [°] | PWM | Position [°] | PWM | Position [°] |
|---|---|---|---|---|---|
| 1000 | 8 | -1300 | 27 | -1300 | 43 |
| -1000 | 8 | 1200 | 29 | 1300 | 49 |
| 1050 | 11 | -1250 | 33 | -1350 | 49 |
| 1150 | 13 | 1250 | 34 | 1350 | 53 |
| 1100 | 19 | -1350 | 37 | -1350 | 53 |
| -1100 | 23 | 1250 | 38 | 1100 | 59 |
| 1150 | 24 | 1300 | 43 | -1200 | 59 |

TABLE 6.1: Sticktion of distal joint

$$\mathrm{F}_F(\theta, \dot{\theta}) = \tau_i - \mathrm{C\_}i - \mathrm{G\_}i$$

The values of $\mathrm{F}_F(\theta, \dot{\theta})$ can be used in a look–up table or finding the parameters for a friction model. In this thesis, look–up tables are used.

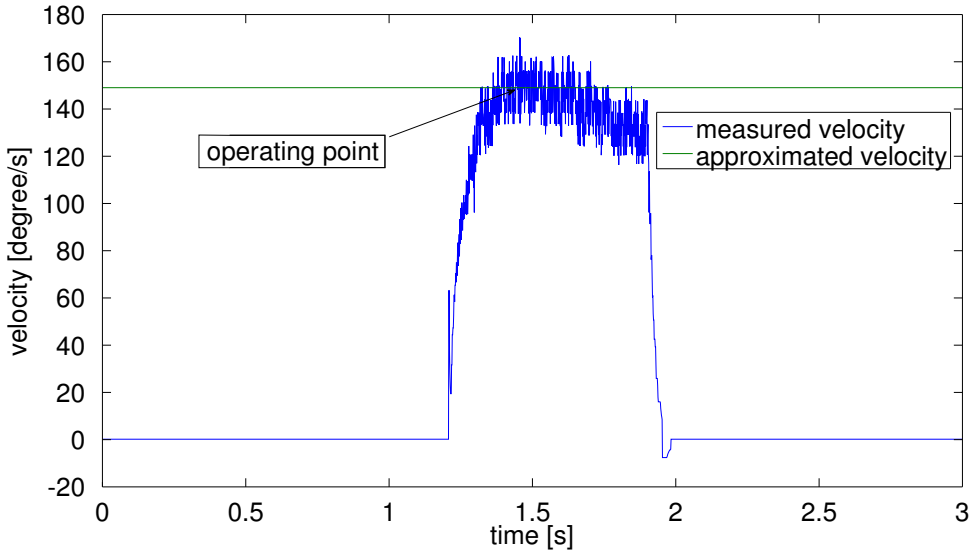


FIGURE 6.3: Velocity of one joint

The first step in modelling the friction was to characterize the stiction. Therefore the distal joint was positioned in steps of 5° over the full movement range and the PWM signal was enhanced in steps of 50 from 500 to 1500. PWM signal, position and velocity where saved in a file. To detect the value at which the finger started moving, the Matlab script shown in Appendix C was written.

The corresponding PWM signals for the stiction of the distal joint are shown in table 6.1. In order to simplify this first model, the mean over the values was built and used to calculate the stiction.

In the base joint, the friction was nearly constant. For both base joints, the stiction was in a range of PWM = 1200 ± 50. That is why, a PWM signal of 1200 was used for every joint, in order to calculate the stiction via the motor model.

The second step was to characterize the dynamic behaviour. Therefore the finger was driven with different PWM signals (1500 . . . 4000 in steps of 50) and the data was logged. The measurements were not carried out in the range of 1200 . . . 1500 PWM signals because undesired Stick–Slip effect occurs and therefore, for grasping and manipulation this range is not useful.

Afterwards wrong measurement points were deleted via Matlab and the maximum velocity and corresponding PWM signals were extracted via Matlab. The Matlab script is shown in Appendix D

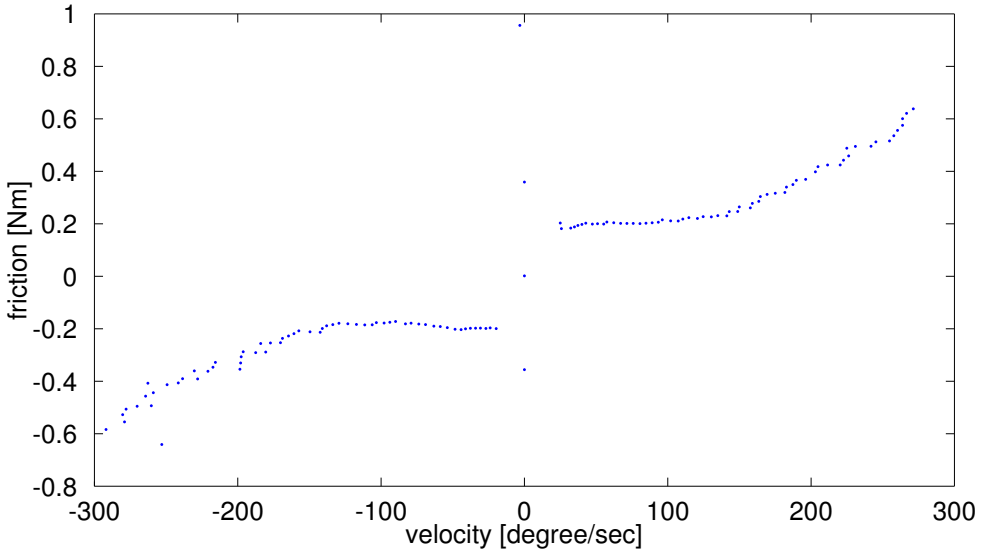


FIGURE 6.4: Friction of the distal joint and added stiction range

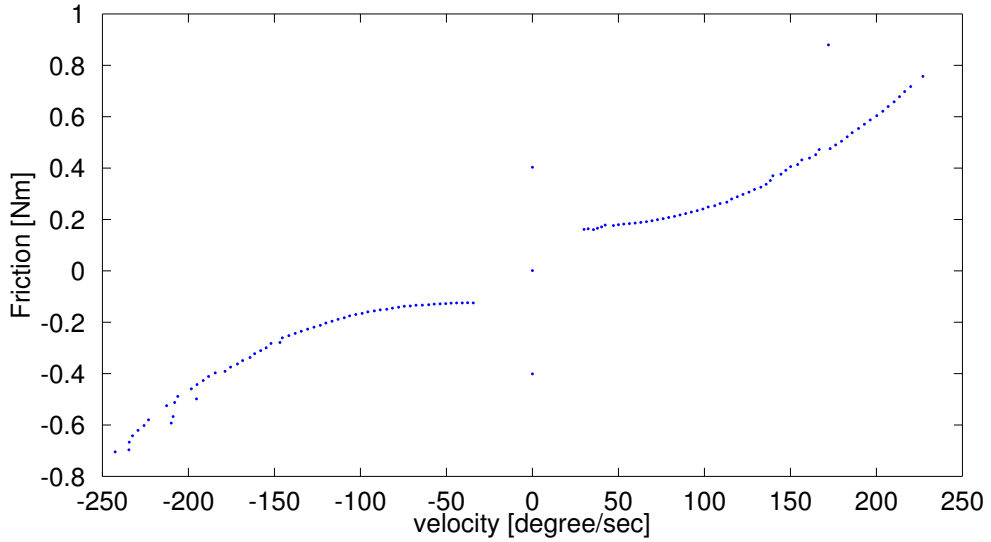


FIGURE 6.5: Friction of base 1 joint and added stiction range

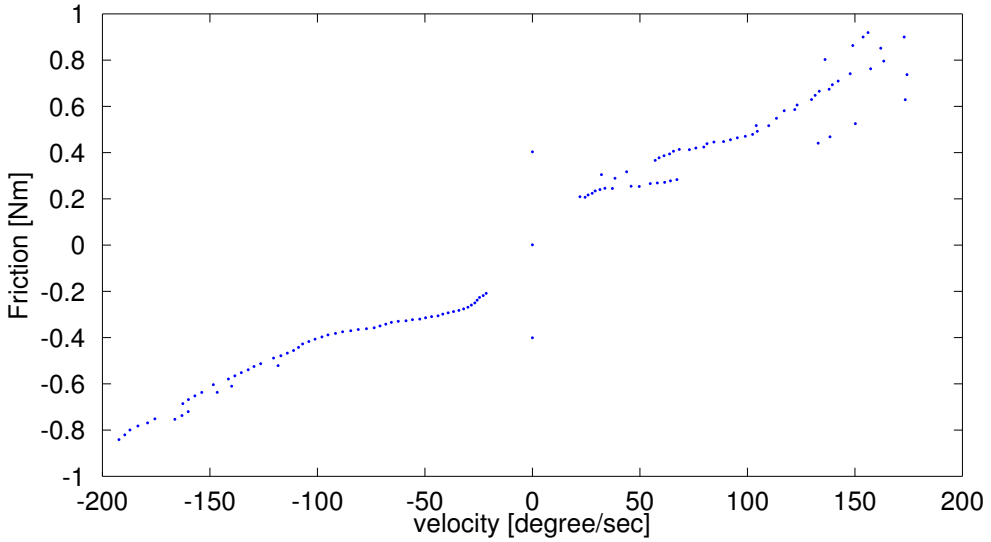


FIGURE 6.6: Friction of base 2 joint and added stiction range, base1 and base2 are mechanically identical the reason for the higher variance of base2 is so far unknown

## 6.3 Conclusion

As shown in figure 6.4, 6.5 and 6.6, the value for stiction is higher than for small velocities which can be explained by the Stribeck effect. The Stribeck model assumes a linear behaviour of the friction for high velocities but in the shown range of the behaviour is not linear.

In figure 6.4 the friction stays constant for small velocities and starts to increase for velocities higher than 150 $^{\circ}/s$. The behaviour in figure 6.6 shows a higher variance than

the other two joints, especially for high velocities. Base 2 is mechanically identical to base 1. The different behaviour can be a result of ageing phenomena of the motor or mechanical abrasion however the exact reason is so far unknown.

For reasons of time, it was decided, to use the measurement points in a look–up table, this also simplifies adaptation of the friction model to other fingers.

Wrong measurement points were neglected and due to the fact, that the base joints are mechanically identical, the measurement values of base 1 are also used for base 2 and if required multiplied with a correcting factor.

The maximum influence of dynamics (equations 4.18, 4.19 and 4.20) is 7.1 mNm while friction has values of (200 . . . 1000) mNm. Therefore the influence of the centrifugal and gravitational term could be neglected to simplify the model. Until it is verified that it is required to enhance the calculation speed to use the model on a real time system, the dynamics will be taken into account. The mass term is required to calculate the resulting acceleration and has to be taken into account.

# Chapter 7

# Complete model

The combination of the models of the motor, dynamics and friction yield to the model of the finger. This model is implemented in Simulink shown in figure 7.1. The input which goes into the model of the motor is the PWM signal. As described in Chapter 5, the torque of the motor depends also on the velocity. A velocity of zero is used for initialization, afterwards the resulting velocity of the finger goes back into the model of the motor and friction. Through an error in the finger model a wrong velocity might be calculated. A high velocity could lead to the situation that the velocity dependent term of the motor model gets bigger than the PWM dependent term. In order to neglect this physically wrong behaviour, the motor model first ensures, that the absolute value of the PWM term is not smaller than the velocity–term. If this is not fulfilled, the produced torque is set to zero. The Matlab code is shown in Appendix E

Due to the fact that the output of the embedded hall sensors is in degree and the unit of the velocity is $\frac{degrees}{second}$, while the unit for the velocity in the motor model is $\frac{rotation}{minutes}$, the velocity of the finger is divided by 360 $\frac{degree}{rotation}$, multiplied by 60 $\frac{seconds}{minute}$ and multiplied with the transmission ratio of the transfer elements.

Additionally, the torque is multiplied by the transmission ratios of the transfer elements and 100 to convert Ncm in Nm. The resulting torque goes as an input into the model of the finger, which includes the friction model.

The finger model shown in Appendix F includes the calculated mass, centrifugal, and gravitational terms from Chapter 4. With these terms and the produced torque of the motor, a variable $tau_$resulting is calculated. This variable includes torque as well as

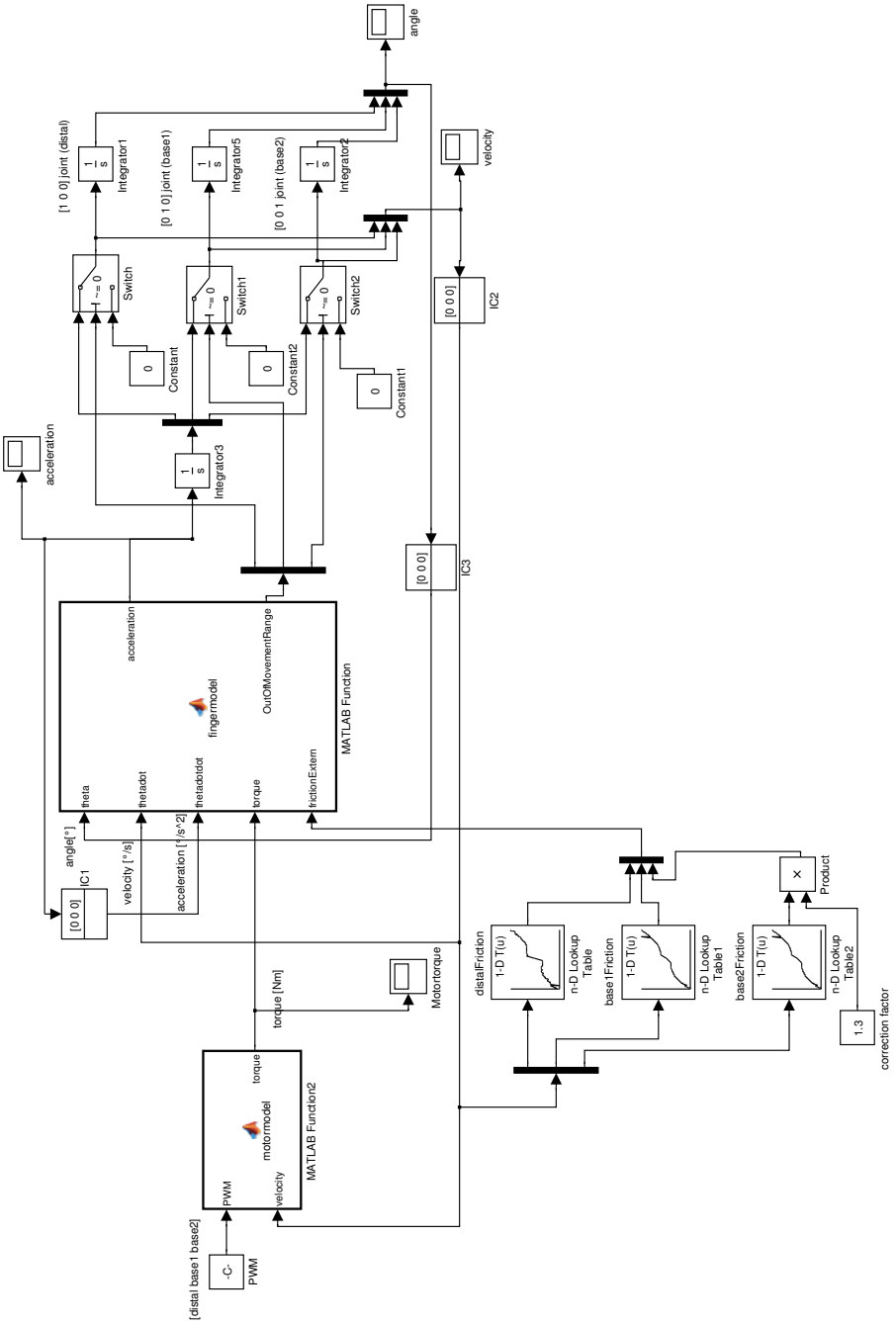


FIGURE 7.1: Complete model implemented in Simulink

the influence of the dynamics. This term is required for the unsteadiness at a velocity of zero. The stiction opposes the value of applied torques which have to be calculated first.

One thing which was not considered so far is that, two different coordinate systems for the base joint were defined. The base joint is modelled as joint 1 and 2 shown in figure 4.2. The real base joint shown in figure 3.3 on the contrary has a bevel gear mechanism.

In figure 7.2 curling/extension of the finger is along $y_2$ which also represents changes in $\theta_2$ in the dynamics, abduction/adduction is along $y_1$ which corresponds to changes in $\theta_1$. The bevel gear mechanism results in a movement in the direction of tau_resulting(1) if the motor of base 1 moves, while moving the motor of base 2 results in the direction of tau_resulting(2) in figure 7.2. To map tau_resulting on the axis of the dynamic equations, tau_resulting is multiplied with the sine respectively cosine of the forming angle ($\pm 45°$).

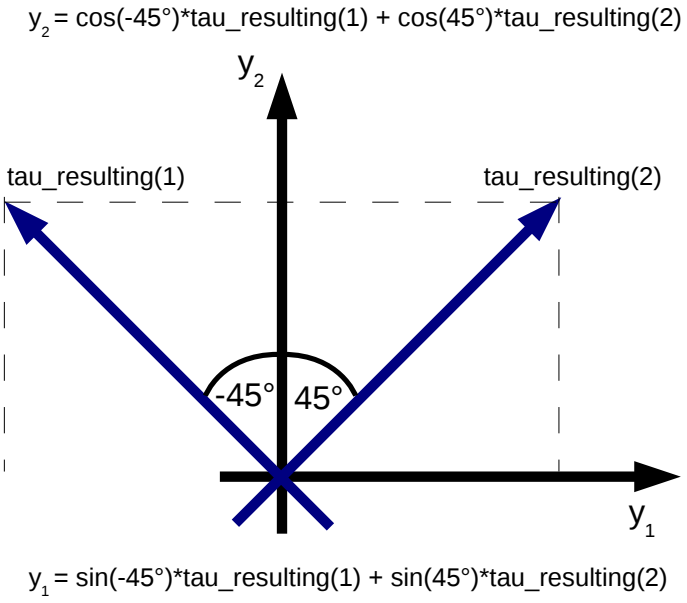


FIGURE 7.2: Motor frame (tau_resulting), dynamics frame($y_1$, $y_2$). The bevel gear mechanism moves the finger in 45° angles to the chosen coordinate system for the dynamics. Therefore tau_resulting) is mapped via sine and cosine on the axis of the dynamics.

The next issue that needs to be taken into account is whether the finger is within its movement range. For this purpose, the "Elseif" fuction from Matlab was used which not only checks if the finger is within the allowed range but also the direction in which the finger is moving. When the finger is out of its movement range the variable OutOf-MovementRange is set to zero and through a "Swich block" the velocity will also be set to zero.

When the finger is within the movement range and the applied torque is bigger than the stiction OutOfMovementRange is set to one. Thereby the calculated velocity is used

and the value for the friction, calculated by the look–up table are activated. The values used in the look–up tables are shown in Appendix G.

The last part of the code calculates the acceleration by subtracting the friction of the resulting torque and divides the result by the mass term. To get the result in degree it is converted by multiplying it with $180/\pi$.

The derivated velocity is fed back into the motor model and the look–up tables. Due to the fact that the measurement values for base joint 2 had a high variance, the look–up table for base 1 is multiplied with a correction factor.

The output of the finger model is the acceleration. The acceleration and its derivatives are fed back into the finger model and the velocity is used as second input for the motor model.

## 7.1 Verification

In order to verify the accuracy of the model, the velocity for different PWM signals is compared to the simulation. Typical values are shown in figure 7.3, 7.4 and 7.5. For reasons of clarity only three typical samples per joint are shown. Additional figures with the comparison of simulation and measured values can be found in H.

The figures show the velocity over time of three different PWM signals for each joint. As illustrated, the acceleration in the beginning of every movement is similar and the absolute velocity differs in the worst case about 25 %. In the braking phase the simulation sets the velocity directly to zero when the finger reaches the end of movement range, hence the simulation shows a vertical slope, while the real finger has a high negative slope. It is assumed, that this slope is a result of the elasticity of the belts. In some of the measurements resilience is shown after the braking.

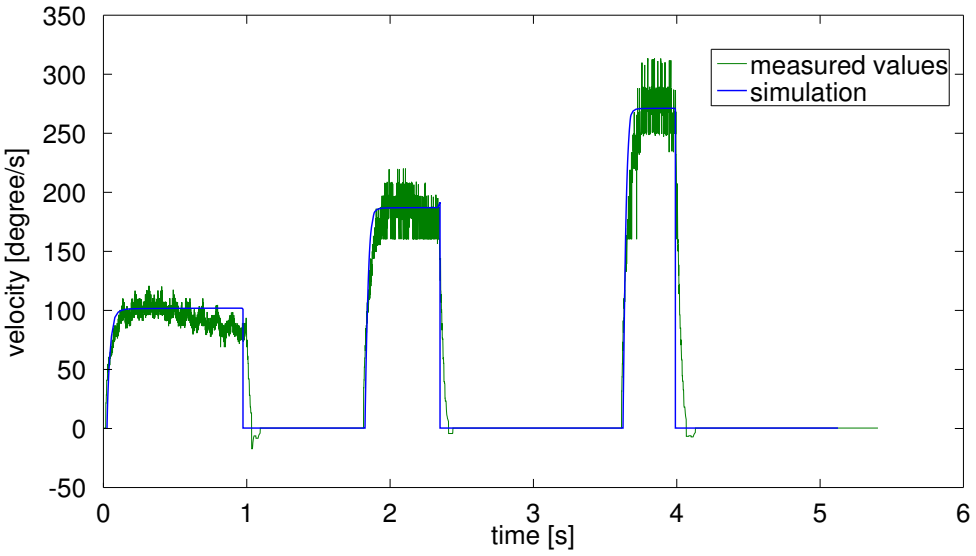


FIGURE 7.3: Verification of the model for the distal joint: The figure shows PWM signal of 2000, 3000, 4000. The measured values (in green) show a braking phase due to the elastic belt while the simulation sets the velocity to zero when the finger reaches the border of movement range.

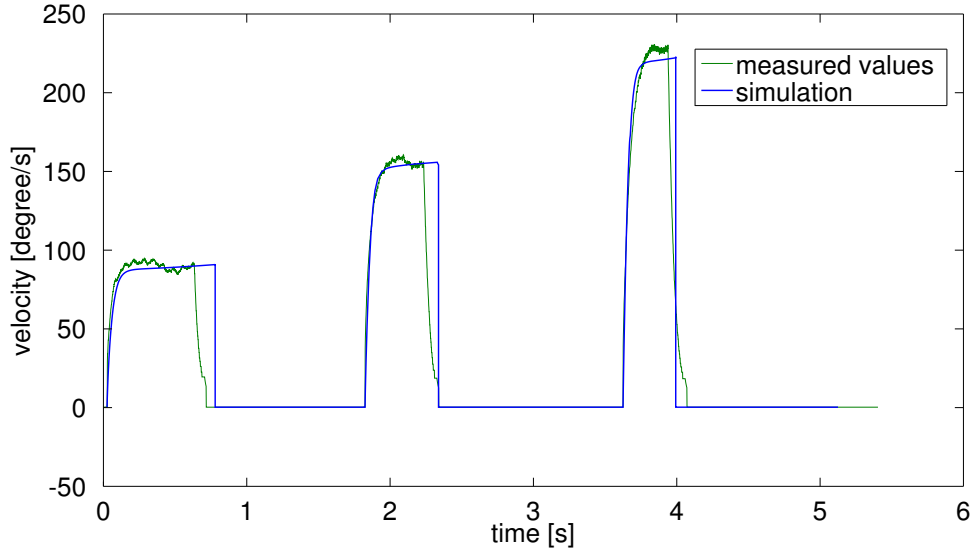


FIGURE 7.4: Verification of the model for base joint 1: The figure shows PWM signal of 2000, 3000, 4000. The measured values (in green) show a braking phase due to the elastic belt while the simulation sets the velocity to zero when the finger reaches the border of movement range.

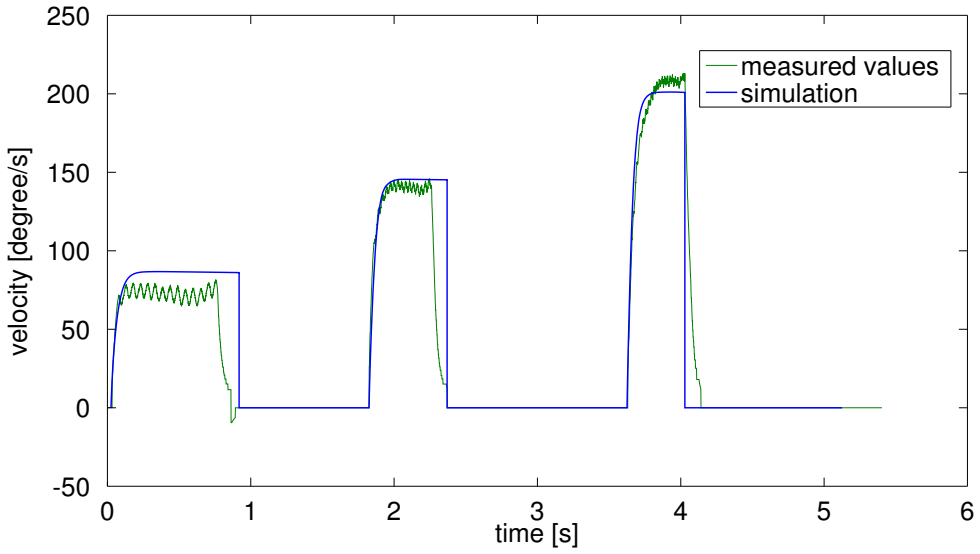


FIGURE 7.5: Verification of the model for base joint 2: The figure shows PWM signal of 2000, 3000, 4000. The measured values (in green) show a braking phase due to the elastic belt while the simulation sets the velocity to zero when the finger reaches the border of movement range.

# Chapter 8

# Conclusion and Outlook

## 8.1 Conclusion

In this work, a first complete dynamic model for the DLR/HIT Hand II was developed. The main components include actuator (BLDC motor) characterization, friction modelling, and finally a set of dynamic equations were obtained.

For the characterization of the motor, a test bed including a torque sensor and a hysteresis brake was constructed. In section 5.2 and 5.4 it was shown and discussed that the torque of the motor is composed of two clearly differentiable terms. One is dependent on PWM input, whereas the other correlates to the rotational speed. Moreover, it was discovered that the slope of the rotational speed dependent term varies with the PWM signal. Due to the fact that it is currently not possible to determine the temperature of the motor with the embedded sensors, a constant operating temperature was assumed. In order to reach operating temperature the hand should be in use for a few minutes prior to actual operation.

Section 3.2.2 showed that modelling of the friction of every component singular is not necessarily beneficial to producing an accurate and usable dynamic model for the robotic finger. Friction was instead treated as a single phenomenon for the entire system. The resulting friction model has been implemented into look-up tables. While friction behaviors of the distal and first base joint mechanisms are similar to the Stribeck model, the second base joint demonstrated a higher variance. As both base joint mechanisms have an identical construction, the cause for the observed higher variance is subject to

speculation. The friction model for the first base was multiplied with a correction factor to be implemented for the second base joint mechanism. The influences of centrifugal and gravitational forces are small compared to the friction, as a result, they may be neglected to help reduce computational resources necessary for the model. However, in order to retain accuracy, they are nonetheless included in this work.

Finally, the model was verified using a comparison between the simulation and experimental velocity measurements. This was the only data available currently for the verification of the dynamic model. More future work would be necessary to help validate the proposed dynamic model in this work.

## 8.2 Outlook

With the completion of the dynamic model of the DLR/HIT II, an array of possibilities for control schemes can be considered. In conjunction with the new controller, further improvements on the model's accuracy could and should be improved. Effective model simplification should also be explored to enhance calculation speed. In order to identify the cause of the higher variance of the friction in the second base joint mechanism, the same experiments should be carried out on more robotic fingers of identical design to eliminate possible anomalies or extend the model to cover systemic differences.

Finally, during the course of this work, several issues, which can improve the model, have been identified for further study:

- Inclusion of elastic elements, as well as the inertias of the transfer elements to help improve the current model.
- Additional temperature sensors may be installed near the motor to cope with motor output as a function of temperature variance.
- Addtional current sensing may also help improve control performance as current is a more direct reflection of actual motor torque than PWM signal.
- As the motor test bed was mounted on Profile Item rapid prototype construction, larger tolerances can cause undesirable misalignment, which in turn reduces motor

output measurement accuracy. A custom high-precision should be designed to replace the current setup.

- Friction behavior in the stiction/slip region should be characterized to help improve the current friction model
- Development of an equation-based friction model instead of the current look-up table may provide a better solution and help improve future controller performance.

# Appendix A

# m-file iterative newton-euler

```
%Dynamics of one finger
%iterative Newton-Euler dynamics algorithm is used
%Equations look "introduction to robotics Mechanics and Control" John J.
%Craig Third Edition.

%finger is modeled by a 4 link manipulator, first link has length zero and
%the first 2 joints are orthogonal on eachother

x=[1 0 0]'; y=[0 1 0]'; z=[0 0 1]'; zerovec = [0 0 0]'; % unit vectors
h1=z; h2=z; h3=z; h4=z; %joint axis
h = [h1, h2, h3, h4]';
h = sym(h); %symbolic toolbox has sometimes problems with different datatypes

syms g m0 m1 m2 m3 N1 N2 N3 N4 Im1m Im2m Im3m Im4m real; %mass of the 3 links
m = [m0 m1 m2 m3]';
syms l0 l1 l2 l3 l0c l0c l1c l2c l3c real
% li = link length, lic = distance joint(i) to center of mass(i)

syms t1 t2 t3 t4 real % theta (jointangle)
syms td1 td2 td3 td4 real %thetadot (angular velocity)
td = [td1*h1 td2*h2 td3*h3 td4*h4];
syms tdd1 tdd2 tdd3 tdd4 real %(angular acceleration)
tdd = [tdd1*h1 tdd2*h2 tdd3*h3 tdd4*h4];

%rotation matrices
Rx = [1 0 0; 0 cosd(-90) -sind(-90); 0 sind(-90) cosd(-90)];
%rotation around x axis 90 deg
Ry = [cosd(90) 0 sind(90); 0 1 0; -sind(90) 0 cosd(90)];
%rotation around y axis 90 deg
Rz = [cosd(90) -sind(90) 0; sind(90) cosd(90) 0; 0 0 1];
%rotation around z axis 90 deg
```

```
R01 = [cos(t1) -sin(t1) 0; sin(t1) cos(t1) 0; 0 0 1]; %rotation around z axis
%rotate joint around 90 deg
R12 = Rx*[cos(t2) -sin(t2) 0; sin(t2) cos(t2) 0; 0 0 1]; %rotation around z axis
R23 = [cos(t3) -sin(t3) 0; sin(t3) cos(t3) 0; 0 0 1]; %rotation around z axis
R34 = [cos(t4) -sin(t4) 0; sin(t4) cos(t4) 0; 0 0 1]; %rotation around z axis
R45 = [1 0 0; 0 1 0; 0 0 1]; %no rotation, last joint to fingertip
R = cat(3,R01, R12, R23, R34, R45);

% x is direction of the link
%p points from joint(i) to joint(i+1)
%pc points from joint to center of mass
p0 = l0*x;
pc0 = l0c*x;
p1 = l1*x;
pc1 = l1c*x;
p2 = l2*x;
pc2 = l2c*x;
p3 = l3*x;
pc3 = l3c*x;

p = cat(3, zerovec, p0, p1, p2, p3); %zerovec added!!!
pc = cat(3, pc0, pc1, pc2, pc3);

%Inertia Tensor = 0 because we assume pointmass
I_c = cat(3, zeros(3), zeros(3),zeros(3),zeros(3));

% 4th joint is coupled with third; motor inertia can only be counted once!
% Imim is motor inertia
%Im1m= 5.1e-07; Im2m= 5.1e-07; Im3m= 5.1e-07; Im4m=0;
Im = cat(3, Im1m*N1^2*h1*transpose(h1), Im2m*N2^2*h2*transpose(h2), ...
 Im3m*N3^2*h3*transpose(h3), Im4m*N4^2*h4*transpose(h4));

I_00 = m0*(pc0' * pc0 * eye(3) - pc0 * pc0');
I_11 = m1*(pc1' * pc1 * eye(3) - pc1 * pc1');
I_22 = m2*(pc2' * pc2 * eye(3) - pc2 * pc2');
I_33 = m3*(pc3' * pc3 * eye(3) - pc3 * pc3');
I = I_c + Im + cat(3, I_00, I_11, I_22, I_33);


%-------------------------------------------------------------------------
%Dynamics
%craig 176

%Outward iteration
%-------------------------------------------------------------------------
omega = sym(zeros(3,1,5));
omegad = sym(zeros(3,1,5));
```

```
vd = sym(zeros(3,1,5));
vd(:,:,1) = y*g; %Gravitation
vcd(:,:,1) = vd(:,:,1);

vcd = sym(zeros(3,1,5));
F = sym(zeros(3,1,5));
N = sym(zeros(3,1,5));

i = 4; % 4 links
    for k=1:i %Newton-Euler-approach, look craig 176
      omega(:,:,k+1) = R(:,:,k)'*omega(:,:,k) + td(:,k);
      %omega(:,:,1) = angular velocity of base frame = 0
      omegad(:,:,k+1) = R(:,:,k)'*omegad(:,:,k) ...
      + cross((R(:,:,k)'*omega(:,:,k)), td(:,k)) + tdd(:,k);
      %omegad(:,:,1) = angular acceleration of base frame = 0
      vd(:,:,k+1) = R(:,:,k)' * (cross(omegad(:,:,k),p(:,:,k))
      + cross(omega(:,:,k), cross(omega(:,:,k),p(:,:,k))) + vd(:,:,k));
       %vd(:,:,1) acceleration of base frame = 0,
       %vd(:,:,2) = 0 because length between joint 1 and 2 is zero
      vcd(:,:,k+1) = cross(omegad(:,:,k+1), pc(:,:,k)) ...
      + cross(omega(:,:,k+1), ...
      (cross(omega(:,:,k+1), pc(:,:,k)))) + vd(:,:,k+1);
      %acceleration of center of mass
      F(:,:,k+1) = m(k) * vcd(:,:,k+1); %force
      N(:,:,k+1) = I(:,:,k) * omegad(:,:,k+1) + cross(omega(:,:,k+1), ...
       (I(:,:,k)*omega(:,:,k+1))); %momentum
    end

%-------------------------------------------------------------------------

%inward iteration
%-------------------------------------------------------------------------
f = sym(zeros(3,1,6));  last column zerovec (no force at fingertip)
n = sym(zeros(3,1,6)); %no mementum at fingertip
torque = sym(zeros(3,1,5));

i = 5;
for k=i:-1:2 %Newton-Euler-approach, look craig 176
    f(:,:,k) = R(:,:,k) *  f(:,:,k+1) + F(:,:,k);  %force
    n(:,:,k) = N(:,:,k) + R(:,:,k)*n(:,:,k+1) + cross(pc(:,:,k-1), F(:,:,k)) ...
    + cross(p(:,:,k), (R(:,:,k) * f(:,:,k+1))); %torque
    torque(:,:,k) = n(:,:,k)' * h(k-1,:)'*h(k-1,:); %torques 1-4

end

TorqueSimp = simplify(torque(:,:,2:5)); %dynamics of a 4-link-manipulator
Tau = [TorqueSimp(3,:,1); TorqueSimp(3,:,2); ...
TorqueSimp(3,:,3) + TorqueSimp(3,:,4)];
```

```
%-------------------------------------------------------------------------

%coupling of distal and proximal joint
Tau2 = subs(Tau, tdd4, tdd3);
Tau2 = subs(Tau2, td4, td3);
Tau2 = subs(Tau2, t4, t3);
%substitution for timing belt

%link0 = 0
Tau2 = subs(Tau2, l0, 0);
Tau2 = subs(Tau2, m0, 0);
Tau2 = subs(Tau2, l0c, 0);
Tau2 = simplify(Tau2);

%mass-term
Tau_M = subs(Tau2, g, 0);
Tau_M = subs(Tau_M, td1, 0);
Tau_M = subs(Tau_M, td2, 0);
Tau_M = subs(Tau_M, td3, 0);
Tau_M = simplify(Tau_M);

collect(Tau_M(1), tdd1)
collect(Tau_M(2), tdd2)
collect(Tau_M(3), tdd3)

%centrifugal term
Tau_C = subs(Tau2, g, 0);
Tau_C = subs(Tau_C, tdd1, 0);
Tau_C = subs(Tau_C, tdd2, 0);
Tau_C = subs(Tau_C, tdd3, 0);
Tau_C = simplify(Tau_C);

%gravity-term
Tau_g = subs(Tau2, tdd1, 0);
Tau_g = subs(Tau_g, tdd2, 0);
Tau_g = subs(Tau_g, tdd3, 0);
Tau_g = subs(Tau_g, td1, 0);
Tau_g = subs(Tau_g, td2, 0);
Tau_g = subs(Tau_g, td3, 0);
Tau_g = simplify(Tau_g);
```

# Appendix B

# results of the implemented newton-euler approach

```
%Mass terms
M_1 = (Im1m*N1^2 + (l2^2*m3)/2 + l2c^2*m2 + l3c^2*m3
+ (l2^2*m3*cos(2*t2 + 2*t3))/2 + l2c^2*m2*cos(2*t2 + 2*t3)
+ l3c^2*m3*cos(2*t2 + 4*t3) + l1^2*m2*cos(t2)^2
+l1^2*m3*cos(t2)^2 + 2*l1c^2*m1*cos(t2)^2
+ l1*l3c*m3*cos(2*t2 + 2*t3) + l2*l3c*m3*cos(2*t2 + 3*t3)
+ l1*l2*m3*cos(t3) + l1*l2c*m2*cos(t3) + l2*l3c*m3*cos(t3)
+ l1*l2*m3*cos(2*t2 + t3) + l1*l2c*m2*cos(2*t2 + t3)
+ l1*l3c*m3*cos(2*t3));

M_2 = (Im2m*N2^2 + Im3m*N3^2 + Im4m*N4^2 + l1^2*m2 + l1^2*m3 + l2^2*m3
+ 2*l1c^2*m1 + 2*l2c^2*m2 + 2*l3c^2*m3 + 2*l1*l2*m3*cos(t3)
+ 2*l1*l2c*m2*cos(t3) + 2*l2*l3c*m3*cos(t3) + 2*l1*l3c*m3*cos(2*t3));

M_3 = (Im3m*N3^2 + 4*Im4m*N4^2 + m3*l2^2 + 4*m3*cos(t3)*l2*l3c + 2*m2*l2c^2
+ 8*m3*l3c^2);

%torque produced by acceleration of other joints
M_1_rest = 0;

M_2_rest = + Im3m*tdd3*N3^2 + 2*Im4m*tdd3*N4^2 + m3*tdd3*l2^2
+ 3*m3*tdd3*cos(t3)*l2*l3c + l1*m3*tdd3*cos(t3)*l2 + 2*m2*tdd3*l2c^2
+ l1*m2*tdd3*cos(t3)*l2c + 4*m3*tdd3*l3c^2 + 2*l1*m3*tdd3*cos(2*t3)*l3c;

M_3_rest = + Im3m*tdd2*N3^2 + 2*Im4m*tdd2*N4^2 + m3*tdd2*l2^2
+ 3*m3*tdd2*cos(t3)*l2*l3c + l1*m3*tdd2*cos(t3)*l2 + 2*m2*tdd2*l2c^2
+ l1*m2*tdd2*cos(t3)*l2c + 4*m3*tdd2*l3c^2 + 2*l1*m3*tdd2*cos(2*t3)*l3c;

%Centrifugal term
```

```
C_1 =  -td1*(l1^2*m2*td2*sin(2*t2) + l1^2*m3*td2*sin(2*t2)
+ 2*l1c^2*m1*td2*sin(2*t2) + l2^2*m3*td2*sin(2*t2 + 2*t3)
+ l2^2*m3*td3*sin(2*t2 + 2*t3) + 2*l2c^2*m2*td2*sin(2*t2 + 2*t3)
+ 2*l2c^2*m2*td3*sin(2*t2 + 2*t3) + 2*l3c^2*m3*td2*sin(2*t2 + 4*t3)
+ 4*l3c^2*m3*td3*sin(2*t2 + 4*t3) + l1*l2*m3*td3*sin(t3)
+ l1*l2c*m2*td3*sin(t3) + l2*l3c*m3*td3*sin(t3) + 2*l1*l2*m3*td2*sin(2*t2
+ t3) + l1*l2*m3*td3*sin(2*t2 + t3) + 2*l1*l2c*m2*td2*sin(2*t2 + t3)
+ l1*l2c*m2*td3*sin(2*t2 + t3) + 2*l1*l3c*m3*td3*sin(2*t3)
+ 2*l1*l3c*m3*td2*sin(2*t2 + 2*t3) + 2*l1*l3c*m3*td3*sin(2*t2 + 2*t3)
+ 2*l2*l3c*m3*td2*sin(2*t2 + 3*t3) + 3*l2*l3c*m3*td3*sin(2*t2 + 3*t3));

C_2 =  (l1^2*m2*td1^2*sin(2*t2))/2 + (l1^2*m3*td1^2*sin(2*t2))/2
+ l1c^2*m1*td1^2*sin(2*t2) + (l2^2*m3*td1^2*sin(2*t2 + 2*t3))/2
+ l2c^2*m2*td1^2*sin(2*t2 + 2*t3) + l3c^2*m3*td1^2*sin(2*t2 + 4*t3)
- l1*l2*m3*td3^2*sin(t3) - l1*l2c*m2*td3^2*sin(t3)
- 3*l2*l3c*m3*td3^2*sin(t3) + l1*l2*m3*td1^2*sin(2*t2 + t3)
+ l1*l2c*m2*td1^2*sin(2*t2 + t3) - 4*l1*l3c*m3*td3^2*sin(2*t3)
+ l1*l3c*m3*td1^2*sin(2*t2 + 2*t3) + l2*l3c*m3*td1^2*sin(2*t2 + 3*t3)
- 2*l1*l2*m3*td2*td3*sin(t3) - 2*l1*l2c*m2*td2*td3*sin(t3)
- 2*l2*l3c*m3*td2*td3*sin(t3) - 4*l1*l3c*m3*td2*td3*sin(2*t3);

C_3 = (l2^2*m3*td1^2*sin(2*t2 + 2*t3))/2 + l2c^2*m2*td1^2*sin(2*t2 + 2*t3)
+ 2*l3c^2*m3*td1^2*sin(2*t2 + 4*t3) + (l1*l2*m3*td1^2*sin(t3))/2
+ l1*l2*m3*td2^2*sin(t3) + (l1*l2c*m2*td1^2*sin(t3))/2
+ l1*l2c*m2*td2^2*sin(t3) + (l2*l3c*m3*td1^2*sin(t3))/2
+ l2*l3c*m3*td2^2*sin(t3) - 2*l2*l3c*m3*td3^2*sin(t3)
+ (l1*l2*m3*td1^2*sin(2*t2 + t3))/2 + (l1*l2c*m2*td1^2*sin(2*t2 + t3))/2
+ l1*l3c*m3*td1^2*sin(2*t3) + 2*l1*l3c*m3*td2^2*sin(2*t3)
+ l1*l3c*m3*td1^2*sin(2*t2 + 2*t3) + (3*l2*l3c*m3*td1^2*sin(2*t2 + 3*t3))/2;

%Gravitational term
G_1 =  g*cos(t1)*(l1*m2*cos(t2) + l1*m3*cos(t2) + l1c*m1*cos(t2)
+ l3c*m3*cos(t2 + 2*t3) + l2*m3*cos(t2 + t3) + l2c*m2*cos(t2 + t3));

G_2 =  -g*sin(t1)*(l1*m2*sin(t2) + l1*m3*sin(t2) + l1c*m1*sin(t2)
+ l3c*m3*sin(t2 + 2*t3) + l2*m3*sin(t2 + t3) + l2c*m2*sin(t2 + t3));

G_3 = -g*sin(t1)*(2*l3c*m3*sin(t2 + 2*t3) + l2*m3*sin(t2 + t3)
+ l2c*m2*sin(t2 + t3));

t1; t2; t3;             angle of joint 1 - 3
td1; td2; td3           rotational velocity of joint 1 - 3
tdd1; tdd2; tdd3        rotational acceleration of joint 1 - 3

g = 9.81:                                       gravitational acceleration
l1 = 55e-03; %m                                 length of proximal phalanges
l2 = 25e-03; %m                                 length of intermediate phalanges
l3 = 25e-03; %m                                 length of distal phalanges
```

```
m1 = 4.4370598e-02; %kg                          mass of Proximal phalanges
m2 = 2.7110192e-02; %kg                          mass Intermediate phalanges
m3 = 1.8179709e-02; %kg                          mass of distal phalanges

pc1 = [3.0164510e-02 -1.0130813e-03 5.0813186e-04]';
vector to center of mass of proximal phalanges
pc2 = [5.7271879e-03 -1.6164173e-03 -1.1567914e-03]';
vector to center of mass of proximal phalanges
pc3 = [6.1007977e-03 -8.3348211e-04 1.7728256e-03]';
vector to center of mass of proximal phalanges

N1=100; N2=100; N3=100; N4=100; transmission of HD-drives

Im1m= 5.1e-07; Im2m= 5.1e-07; Im3m= 5.1e-07;    inertias of the motors
```

# Appendix C

# stiction

```
data = load('/media/Transcend/pdffiles/log_1'); %load data from log-file
data = data(:, [1,7,22]);
%choose columns for PWM-Signal(1), position(7), velocity(22)

n = length(data);

%delete false sensor signals
for i = 2:n
    if(abs(data(i,2))>100)      %valid positions are 0 - 60 degree
        data(i,2) = data(i-1,2);
    end
        if(abs(data(i,3))>400)  %valid velocities are +/- 0 - 200 degree/sec
        data(i,3) = data(i-1,3);
    end

end


data_2 = [0 0]; %variable for PWM-Signal and velocity
counter = 0;

for i = 500:10:n-500

    if((data(i+10,1) ~= 0) & (data(i,1) == 0)) %Flanke start PWM

        PWM_start = i;
        counter = counter+1;
    end

    if((data(i+10,1) == 0) & (data(i,1) ~= 0)) %Flanke stop PWM
        PWM_stop = i;
        counter = counter+1;
```

```
    end

    if(counter == 2)
        counter = 0;
        summe = sum(data(PWM_start:PWM_stop,3)~=0);

        if(summe>1000)  %if more then 1000 values of velocity ~= 0
        PWM = data(PWM_start+10 ,1);
        posi = data(PWM_start+10,2);

        data_2 = [data_2; PWM, posi];
        end
    end

end
```

# Appendix D

# dynamic friction

```
data = load('log_1dyn');

data = data(:, [1,7,22]);
%chooses columns for PWM, position and velocity of corresponding joint
n = length(data);

for i = 2:n
    if(abs(data(i,2))>100)              %deletes wrong positions
        data(i,2) = data(i-1,2);
    end
        if(abs(data(i,3))>400)          %deletes wrong velocities
        data(i,3) = data(i-1,3);
    end

end

data_2 = [];
counter = 0;
for i = 500:10:n-500

    if((data(i+10,1) ~= 0) & (data(i,1) == 0)) %PWM started

        PWM_start = i;
        counter = counter+1;
    end

    if((data(i+10,1) == 0) & (data(i,1) ~= 0)) %PWM stopped
        PWM_stop = i;
        counter = counter+1;
    end

    if(counter == 2)
```

```
        counter = 0;
        [a, b] = max(abs(data(PWM_start:PWM_stop,3)));
        PWM = data(PWM_start+b,1);
        posi = data(PWM_start+b,2);
        vel = mean(data(PWM_start+b-50:PWM_start+b+50, 3));
        data_2 = [data_2; PWM, posi, vel];
    end

end
```

# Appendix E

# motormodel

---

```
function torque  = motormodel(PWM, velocity)
%#codegen

var = [0 0 0];

%distal joint
if(abs(1.43*10^-4 .*PWM(1)) < abs((1.215*10^(-8) .* abs(PWM(1)) - 7.711*10^(-5))
 .*((velocity(1) .*60 .* 100 .* 2.083)./360)))
    var(1) = 0;
else
var(1) = (1.43*10^-4 .*PWM(1) + (1.215*10^(-8) .* abs(PWM(1)) - 7.711*10^(-5))
 .*((velocity(1) .*60 .* 100 .* 2.083)./360)) .*100* 2.083; %motortorque * HD
 * belt
end


if(abs(1.43*10^-4 .*PWM(2)) < abs((1.215*10^(-8) .* abs(PWM(2)) - 7.711*10^(-5))
 .*((velocity(2) .*60 .* 100 .* 2.083 .* 1.125)./360)))
    var(2) = 0;
else
var(2) = (1.43*10^-4 .*PWM(2) + (1.215*10^(-8) .* abs(PWM(2)) - 7.711*10^(-5))
 .*((velocity(2) .*60 .* 100 .* 2.083 .* 1.125)./360)) .*100 * 2.083 * 1.125;
  %motortorque * HD * belt1 * belt2
end

if(abs(1.43*10^-4 .*PWM(3)) < abs((1.215*10^(-8) .* abs(PWM(3)) - 7.711*10^(-5))
 .*((velocity(3) .*60 .* 100 .* 2.083 .* 1.125)./360)))
    var(3) = 0;
else
var(3) = (1.43*10^-4 .*PWM(3) + (1.215*10^(-8) .* abs(PWM(3)) - 7.711*10^(-5))
 .*((velocity(3) .*60 .* 100 .* 2.083 .* 1.125)./360)) .*100 * 2.083 .* 1.125;
```

```
  %motortorque*HD*belt
end

torque = var./100; %Ncm to Nm
```

Listing E.1: motormodel

# Appendix F

# fingermodel

```
function [acceleration, OutOfMovementRange]  =
fingermodel(theta, thetadot, thetadotdot,torque, frictionExtern)
%inputs [degree] [degree/s] [degree/s^2] [Nm]

%define fingerparameters
tdd = [0 0 0]';
g = 9.81;

l1 = 55e-03; %m
l2 = 25e-03; %m
l3 = 25e-03; %m
m1 = 4.4370598e-02; %kg
m2 = 2.7110192e-02; %kg
m3 = 1.8179709e-02; %kg
pc1 = [3.0164510e-02 -1.0130813e-03 5.0813186e-04]';
pc2 = [5.7271879e-03 -1.6164173e-03 -1.1567914e-03]';
pc3 = [6.1007977e-03 -8.3348211e-04 1.7728256e-03]';
l1c = norm(pc1);
l2c = norm(pc2);
l3c = norm(pc3);

%N_distal = 2.083; %transmission ratio for distal joint
%N_t_belt_ratio = 1.125; %for base joint t1/(N_distal*N_t_belt_ratio)
N1=100; N2=100; N3=100; N4=100;
Im1m= 5.1e-07; Im2m= 5.1e-07; Im3m= 5.1e-07; Im4m=0;

t1 = theta(1) .* pi/180;
t2 = theta(2) .* pi/180;
t3 = theta(3) .* pi/180;
td1 = thetadot(1) .* pi/180; %degree to rad
td2 = thetadot(2) .* pi/180; %degree to rad
td3 = thetadot(3) .* pi/180; %degree to rad
```

```
tdd1 = thetadotdot(1).* pi/180; %degree to rad
tdd2 = thetadotdot(2).* pi/180; %degree to rad
tdd3 = thetadotdot(3).* pi/180; %degree to rad

%Mass terms
M1 = (Im1m*N1^2 + (l2^2*m3)/2 + l2c^2*m2 + l3c^2*m3
+ (l2^2*m3*cos(2*t2 + 2*t3))/2 + l2c^2*m2*cos(2*t2 + 2*t3)
+ l3c^2*m3*cos(2*t2 + 4*t3) + l1^2*m2*cos(t2)^2
+ l1^2*m3*cos(t2)^2 + 2*l1c^2*m1*cos(t2)^2 + l1*l3c*m3*cos(2*t2
+ 2*t3) + l2*l3c*m3*cos(2*t2 + 3*t3) + l1*l2*m3*cos(t3)
+ l1*l2c*m2*cos(t3) + l2*l3c*m3*cos(t3) + l1*l2*m3*cos(2*t2 + t3)
+ l1*l2c*m2*cos(2*t2 + t3) + l1*l3c*m3*cos(2*t3));

M2 = (Im2m*N2^2 + Im3m*N3^2 + Im4m*N4^2 + l1^2*m2 + l1^2*m3
+ l2^2*m3 + 2*l1c^2*m1 + 2*l2c^2*m2 + 2*l3c^2*m3
+ 2*l1*l2*m3*cos(t3) + 2*l1*l2c*m2*cos(t3) + 2*l2*l3c*m3*cos(t3)
+ 2*l1*l3c*m3*cos(2*t3));

M3 = (Im3m*N3^2 + 4*Im4m*N4^2 + m3*l2^2 + 4*m3*cos(t3)*l2*l3c
+ 2*m2*l2c^2 + 8*m3*l3c^2);

%torque produced by acceleration of other joints
M1_rest = 0;
M2_rest = + Im3m*tdd3*N3^2 + 2*Im4m*tdd3*N4^2 + m3*tdd3*l2^2
+ 3*m3*tdd3*cos(t3)*l2*l3c + l1*m3*tdd3*cos(t3)*l2
+ 2*m2*tdd3*l2c^2 + l1*m2*tdd3*cos(t3)*l2c + 4*m3*tdd3*l3c^2
+ 2*l1*m3*tdd3*cos(2*t3)*l3c;

M3_rest = + Im3m*tdd2*N3^2 + 2*Im4m*tdd2*N4^2 + m3*tdd2*l2^2
+ 3*m3*tdd2*cos(t3)*l2*l3c + l1*m3*tdd2*cos(t3)*l2
+ 2*m2*tdd2*l2c^2 + l1*m2*tdd2*cos(t3)*l2c + 4*m3*tdd2*l3c^2
+ 2*l1*m3*tdd2*cos(2*t3)*l3c;

%Centrifugal term
C1 =  -td1*(l1^2*m2*td2*sin(2*t2) + l1^2*m3*td2*sin(2*t2)
+ 2*l1c^2*m1*td2*sin(2*t2) + l2^2*m3*td2*sin(2*t2 + 2*t3)
+ l2^2*m3*td3*sin(2*t2 + 2*t3) + 2*l2c^2*m2*td2*sin(2*t2 + 2*t3)
+ 2*l2c^2*m2*td3*sin(2*t2 + 2*t3) + 2*l3c^2*m3*td2*sin(2*t2
+ 4*t3) + 4*l3c^2*m3*td3*sin(2*t2 + 4*t3) + l1*l2*m3*td3*sin(t3)
+ l1*l2c*m2*td3*sin(t3) + l2*l3c*m3*td3*sin(t3)
+ 2*l1*l2*m3*td2*sin(2*t2 + t3) + l1*l2*m3*td3*sin(2*t2 + t3)
+ 2*l1*l2c*m2*td2*sin(2*t2 + t3) + l1*l2c*m2*td3*sin(2*t2 + t3)
+ 2*l1*l3c*m3*td3*sin(2*t3) + 2*l1*l3c*m3*td2*sin(2*t2 + 2*t3)
+ 2*l1*l3c*m3*td3*sin(2*t2 + 2*t3) + 2*l2*l3c*m3*td2*sin(2*t2
+ 3*t3) + 3*l2*l3c*m3*td3*sin(2*t2 + 3*t3));

C2 =  (l1^2*m2*td1^2*sin(2*t2))/2 + (l1^2*m3*td1^2*sin(2*t2))/2
```

```
+ l1c^2*m1*td1^2*sin(2*t2) + (l2^2*m3*td1^2*sin(2*t2 + 2*t3))/2
+ l2c^2*m2*td1^2*sin(2*t2 + 2*t3) + l3c^2*m3*td1^2*sin(2*t2
+ 4*t3) - l1*l2*m3*td3^2*sin(t3) - l1*l2c*m2*td3^2*sin(t3)
- 3*l2*l3c*m3*td3^2*sin(t3) + l1*l2*m3*td1^2*sin(2*t2 + t3)
+ l1*l2c*m2*td1^2*sin(2*t2 + t3) - 4*l1*l3c*m3*td3^2*sin(2*t3)
+ l1*l3c*m3*td1^2*sin(2*t2 + 2*t3) + l2*l3c*m3*td1^2*sin(2*t2
+ 3*t3) - 2*l1*l2*m3*td2*td3*sin(t3) - 2*l1*l2c*m2*td2*td3*sin(t3)
- 2*l2*l3c*m3*td2*td3*sin(t3) - 4*l1*l3c*m3*td2*td3*sin(2*t3);

C3 = (l2^2*m3*td1^2*sin(2*t2 + 2*t3))/2 + l2c^2*m2*td1^2*sin(2*t2 + 2*t3)
+ 2*l3c^2*m3*td1^2*sin(2*t2 + 4*t3)
+ (l1*l2*m3*td1^2*sin(t3))/2 + l1*l2*m3*td2^2*sin(t3)
+ (l1*l2c*m2*td1^2*sin(t3))/2 + l1*l2c*m2*td2^2*sin(t3)
+ (l2*l3c*m3*td1^2*sin(t3))/2 + l2*l3c*m3*td2^2*sin(t3)
- 2*l2*l3c*m3*td3^2*sin(t3) + (l1*l2*m3*td1^2*sin(2*t2 + t3))/2
+ (l1*l2c*m2*td1^2*sin(2*t2 + t3))/2 + l1*l3c*m3*td1^2*sin(2*t3)
+ 2*l1*l3c*m3*td2^2*sin(2*t3) + l1*l3c*m3*td1^2*sin(2*t2 + 2*t3)
+ (3*l2*l3c*m3*td1^2*sin(2*t2 + 3*t3))/2;

%Gravitational term
G1 =  g*cos(t1)*(l1*m2*cos(t2) + l1*m3*cos(t2) + l1c*m1*cos(t2)
+ l3c*m3*cos(t2 + 2*t3) + l2*m3*cos(t2 + t3) + l2c*m2*cos(t2
+ t3));
G2 =  -g*sin(t1)*(l1*m2*sin(t2) + l1*m3*sin(t2) + l1c*m1*sin(t2)
+ l3c*m3*sin(t2 + 2*t3) + l2*m3*sin(t2 + t3) + l2c*m2*sin(t2 + t3));

G3 = -g*sin(t1)*(2*l3c*m3*sin(t2 + 2*t3) + l2*m3*sin(t2 + t3)
+ l2c*m2*sin(t2 + t3));



%Frictionmodel
%tau_resulting = torque - M_rest - C*thetadot - G*theta
tau_resulting = [0 0 0];

alpha = pi/4; %movement angle of base joint

tau_resulting(1) = torque(1) - M3_rest - C3 - G3;

tau_resulting2_x = torque(2) .* sin(alpha);
tau_resulting2_y = torque(2) .* cos(alpha);
tau_resulting3_x = torque(3) .* sin(-alpha);
tau_resulting3_y = torque(3) .* cos(alpha);

tau_resulting(2) = (tau_resulting2_x + tau_resulting3_x - M1_rest - C1 - G1;
tau_resulting(3) = (tau_resulting2_y + tau_resulting3_y - M2_rest - C2 - G2;

stribeck = [0 0 0];
stiction = [0.36 0.36 0.36];
```

```
OutOfMovementRange = [0 0 0]';

%%%%%%%%%%%%%%%%%%%%%%%%%%%%%%%%%%%%%%%%%%%%%%%%%%%%%%%%%%%%%%%%%%%%%%%%%%%%%%%
%friction distal joint

if ((tau_resulting(1) <= stiction(1)) && (thetadot(1) == 0))
    stribeck(1) = tau_resulting(1);
elseif(theta(1)<5 && thetadot(1)<0)
    OutOfMovementRange(1) = 0;
    %stribeck(1) = tau_resulting(1);
elseif(theta(1)>90 && thetadot(1)>(-0.1))
    OutOfMovementRange(1) = 0;
    %stribeck(1) = tau_resulting(1);
else
    OutOfMovementRange(1) = 1;
    stribeck(1) = frictionExtern(1);
end
%%%%%%%%%%%%%%%%%%%%%%%%%%%%%%%%%%%%%%%%%%%%%%%%%%%%%%%%%%%%%%%%%%%%%%%%%%%%%%%
%friction base1 joint

if ((tau_resulting(2) <= stiction(2)) && (thetadot(2) == 0))
    stribeck(2) = tau_resulting(2);
elseif(theta(2)<5 && thetadot(2)<0)
    OutOfMovementRange(2) = 0;
%    stribeck(2) = tau_resulting(2);
elseif(theta(2)>90 && thetadot(2)>(-0.1))
    OutOfMovementRange(2) = 0;
%    stribeck(2) = tau_resulting(2);
else
    OutOfMovementRange(2) = 1;
    stribeck(2) = frictionExtern(2);
end
%%%%%%%%%%%%%%%%%%%%%%%%%%%%%%%%%%%%%%%%%%%%%%%%%%%%%%%%%%%%%%%%%%%%%%%%%%%%%%%
%friction base2 joint

if ((tau_resulting(3) <= stiction(3))  && (thetadot(3) == 0))
    stribeck(3) = tau_resulting(3);
elseif(theta(3)<5 && thetadot(3)<0)
    OutOfMovementRange(3) = 0;
%    stribeck(3) = tau_resulting(3);
elseif(theta(3)>90 && thetadot(3)>(-0.1))
    OutOfMovementRange(3) = 0;
%    stribeck(3) = tau_resulting(3);
else
    OutOfMovementRange(3) = 1;
    stribeck(3) = frictionExtern(3);
end
%%%%%%%%%%%%%%%%%%%%%%%%%%%%%%%%%%%%%%%%%%%%%%%%%%%%%%%%%%%%%%%%%%%%%%%%%%%%%%%
```

```
friction = stribeck; % Nm

%-----------------------------------------------------------------------


tdd(1) = 180./pi .* (tau_resulting(1) - friction(1))./(M3);
tdd(2) = 180./pi .* (tau_resulting(2) - friction(2))./(M1);
tdd(3) = 180./pi .* (tau_resulting(3) - friction(3))./(M2);

acceleration = tdd;
```

Listing F.1: fingermodel

# Appendix G

# data used in lookup table

| Breakpoints distal | Data distal | Breakpoints base | Data base |
|---|---|---|---|
| 0 | 0 | -242.6000 | -0.7056 |
| -291.9000 | -0.5855 | -234.6000 | -0.6977 |
| -280.3000 | -0.5290 | -234.4000 | -0.6681 |
| -279.0000 | -0.5565 | -232.5000 | -0.6431 |
| -277.9000 | -0.5079 | -229.3000 | -0.6219 |
| -270.2000 | -0.4969 | -225.8000 | -0.6031 |
| -264.3000 | -0.4584 | -223.2000 | -0.5809 |
| -262.7000 | -0.4091 | -212.7000 | -0.5259 |
| -260.3000 | -0.4950 | -210.0000 | -0.5935 |
| -258.9000 | -0.4453 | -208.9000 | -0.5683 |
| -253.0000 | -0.6426 | -208.0000 | -0.5134 |
| -249.3000 | -0.4147 | -206.2000 | -0.4898 |
| -241.5000 | -0.4080 | -198.3000 | -0.4604 |
| -238.5000 | -0.3919 | -195.3000 | -0.4995 |
| -230.3000 | -0.3621 | -195.0000 | -0.4436 |
| -228.0000 | -0.3928 | -191.4000 | -0.4280 |
| -220.8000 | -0.3636 | -188.3000 | -0.4120 |
| -217.3000 | -0.3482 | -184.4000 | -0.3982 |
| -215.6000 | -0.3297 | -178.7000 | -0.3922 |
| -198.5000 | -0.3558 | -175.5000 | -0.3758 |
| -198.0000 | -0.3320 | -171.5000 | -0.3635 |

| | | | |
|---|---|---|---|
| -197.6000 | -0.3084 | -168.5000 | -0.3503 |
| -196.2000 | -0.2893 | -164.2000 | -0.3384 |
| -187.5000 | -0.2926 | -161.5000 | -0.3235 |
| -184.0000 | -0.2578 | -158.0000 | -0.3116 |
| -180.5000 | -0.2904 | -154.8000 | -0.3006 |
| -177.2000 | -0.2557 | -152.0000 | -0.2838 |
| -170.2000 | -0.2547 | -146.8000 | -0.2799 |
| -168.8000 | -0.2382 | -145.4000 | -0.2619 |
| -164.6000 | -0.2291 | -141.6000 | -0.2533 |
| -160.8000 | -0.2203 | -137.9000 | -0.2444 |
| -157.4000 | -0.2095 | -134.4000 | -0.2363 |
| -149.6000 | -0.2133 | -130.7000 | -0.2279 |
| -142.5000 | -0.2150 | -127.0000 | -0.2203 |
| -141.0000 | -0.2006 | -123.3000 | -0.2131 |
| -138.0000 | -0.1903 | -120.1000 | -0.2041 |
| -133.7000 | -0.1858 | -116.5000 | -0.1972 |
| -129.4000 | -0.1807 | -113.0000 | -0.1897 |
| -123.2000 | -0.1825 | -109.4000 | -0.1837 |
| -117.2000 | -0.1850 | -106.3000 | -0.1763 |
| -111.4000 | -0.1869 | -102.7000 | -0.1710 |
| -106.2000 | -0.1864 | -99.0000 | -0.1666 |
| -103.3000 | -0.1782 | -95.7000 | -0.1607 |
| -97.9000 | -0.1798 | -91.9000 | -0.1570 |
| -93.9000 | -0.1769 | -88.5000 | -0.1529 |
| -89.9000 | -0.1739 | -84.7000 | -0.1507 |
| -83.0000 | -0.1829 | -81.4000 | -0.1462 |
| -79.1000 | -0.1803 | -77.8000 | -0.1426 |
| -73.7000 | -0.1836 | -74.5000 | -0.1389 |
| -69.0000 | -0.1856 | -71.0000 | -0.1379 |
| -63.2000 | -0.1916 | -67.7000 | -0.1349 |
| -58.7000 | -0.1931 | -64.0000 | -0.1346 |
| -53.8000 | -0.1973 | -60.3000 | -0.1328 |
| -48.4000 | -0.2035 | -57.1000 | -0.1305 |

| | | | |
|---|---|---|---|
| -44.2000 | -0.2049 | -53.7000 | -0.1296 |
| -41.1000 | -0.2018 | -50.4000 | -0.1286 |
| -37.7000 | -0.1997 | -47.3000 | -0.1268 |
| -34.1000 | -0.1994 | -44.1000 | -0.1259 |
| -30.7000 | -0.1991 | -40.8000 | -0.1259 |
| -26.9000 | -0.2004 | -37.7000 | -0.1252 |
| -23.9000 | -0.1983 | -34.4000 | -0.1259 |
| -19.7000 | -0.2010 | 0 | 0 |
| 0 | 0 | 30.0000 | 0.1603 |
| 25.0000 | 0.2014 | 32.4000 | 0.1626 |
| 25.8000 | 0.1800 | 35.5000 | 0.1593 |
| 32.3000 | 0.1821 | 37.8000 | 0.1648 |
| 34.9000 | 0.1865 | 40.2000 | 0.1700 |
| 37.3000 | 0.1921 | 42.3000 | 0.1771 |
| 40.1000 | 0.1961 | 47.1000 | 0.1753 |
| 42.8000 | 0.2008 | 50.0000 | 0.1786 |
| 47.4000 | 0.1973 | 53.1000 | 0.1811 |
| 51.0000 | 0.1987 | 56.4000 | 0.1828 |
| 55.3000 | 0.1974 | 59.7000 | 0.1849 |
| 57.5000 | 0.2052 | 63.0000 | 0.1874 |
| 62.3000 | 0.2024 | 66.3000 | 0.1902 |
| 67.1000 | 0.2001 | 69.5000 | 0.1940 |
| 71.5000 | 0.1998 | 72.7000 | 0.1980 |
| 75.9000 | 0.1999 | 76.0000 | 0.2020 |
| 80.6000 | 0.1991 | 79.2000 | 0.2068 |
| 84.8000 | 0.2007 | 82.6000 | 0.2109 |
| 89.1000 | 0.2023 | 85.8000 | 0.2164 |
| 93.4000 | 0.2043 | 89.1000 | 0.2218 |
| 96.2000 | 0.2135 | 92.4000 | 0.2276 |
| 102.0000 | 0.2096 | 95.8000 | 0.2332 |
| 107.3000 | 0.2091 | 99.1000 | 0.2396 |
| 110.5000 | 0.2164 | 102.2000 | 0.2476 |
| 114.7000 | 0.2218 | 106.0000 | 0.2524 |

| | | | |
|---|---|---|---|
| 120.7000 | 0.2188 | 109.1000 | 0.2608 |
| 124.7000 | 0.2257 | 113.0000 | 0.2663 |
| 130.4000 | 0.2248 | 115.8000 | 0.2785 |
| 134.9000 | 0.2295 | 119.1000 | 0.2873 |
| 141.2000 | 0.2287 | 122.4000 | 0.2964 |
| 142.9000 | 0.2449 | 125.9000 | 0.3053 |
| 148.8000 | 0.2453 | 129.1000 | 0.3157 |
| 149.9000 | 0.2628 | 132.8000 | 0.3244 |
| 157.6000 | 0.2591 | 135.9000 | 0.3358 |
| 159.0000 | 0.2762 | 138.3000 | 0.3506 |
| 163.5000 | 0.2839 | 139.8000 | 0.3689 |
| 164.6000 | 0.3022 | 144.5000 | 0.3751 |
| 169.3000 | 0.3104 | 147.3000 | 0.3904 |
| 175.0000 | 0.3148 | 150.1000 | 0.4046 |
| 181.7000 | 0.3178 | 154.2000 | 0.4127 |
| 182.8000 | 0.3382 | 156.6000 | 0.4306 |
| 187.3000 | 0.3479 | 161.1000 | 0.4379 |
| 189.7000 | 0.3641 | 164.7000 | 0.4511 |
| 196.2000 | 0.3678 | 166.7000 | 0.4711 |
| 203.0000 | 0.3965 | 172.1000 | 0.7243 |
| 204.8000 | 0.4162 | 173.1000 | 0.4746 |
| 211.5000 | 0.4225 | 176.3000 | 0.4890 |
| 220.3000 | 0.4227 | 179.7000 | 0.5035 |
| 222.6000 | 0.4408 | 183.0000 | 0.5206 |
| 224.9000 | 0.4865 | 185.9000 | 0.5366 |
| 226.2000 | 0.4571 | 189.6000 | 0.5531 |
| 230.9000 | 0.4934 | 193.0000 | 0.5697 |
| 241.8000 | 0.4939 | 196.4000 | 0.5863 |
| 245.2000 | 0.5106 | 200.2000 | 0.6028 |
| 254.7000 | 0.5142 | 203.7000 | 0.6201 |
| 257.7000 | 0.5340 | 206.8000 | 0.6385 |
| 260.3000 | 0.5544 | 210.3000 | 0.6569 |
| 263.8000 | 0.5737 | 213.4000 | 0.6769 |

| | | | |
|---|---|---|---|
| 263.9000 | 0.5990 | 216.4000 | 0.6968 |
| 266.6000 | 0.6193 | 219.9000 | 0.7164 |
| 271.3000 | 0.6365 | 227.0000 | 0.7558 |

Table G.1: Data of lookup tables

# Appendix H

# additional samples for verification

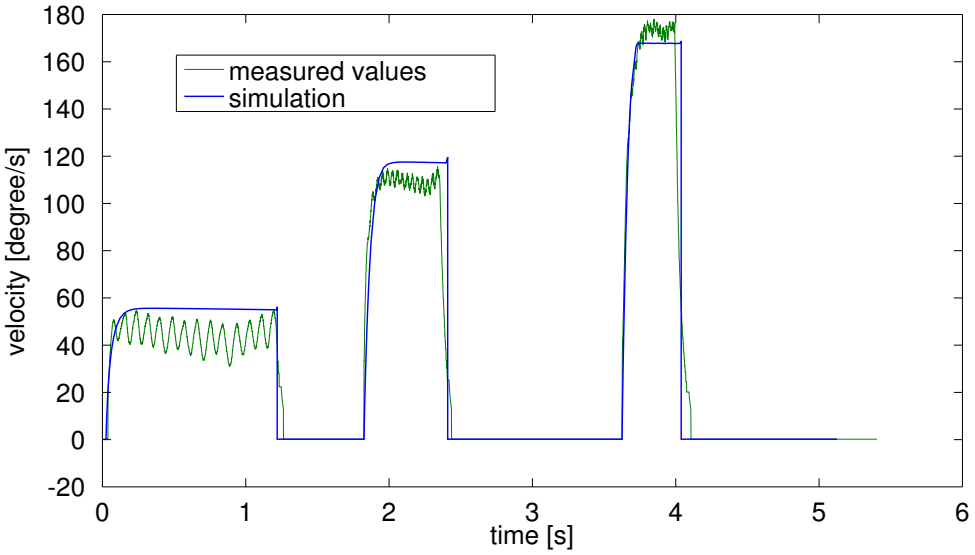


FIGURE H.1: Second verification of base joint 2: The measured values (in green) show a braking phase due to the elastic belt while the simulation (in blue) sets the velocity to zero when the finger reaches the border of movement range. The shown PWM signal are 1500, 2500 and 3500.

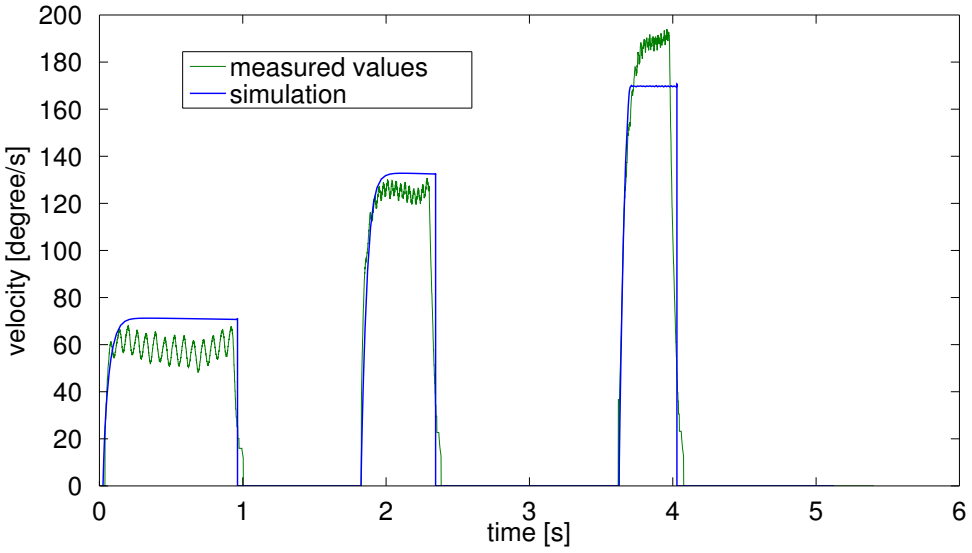


FIGURE H.2: Third verification of base joint 2: The measured values (in green) show a braking phase due to the elastic belt while the simulation (in blue) sets the velocity to zero when the finger reaches the border of movement range. The shown PWM signal are 1750 2750 and 3750. The biggest difference between simulation and measurement is for a signal of 3750

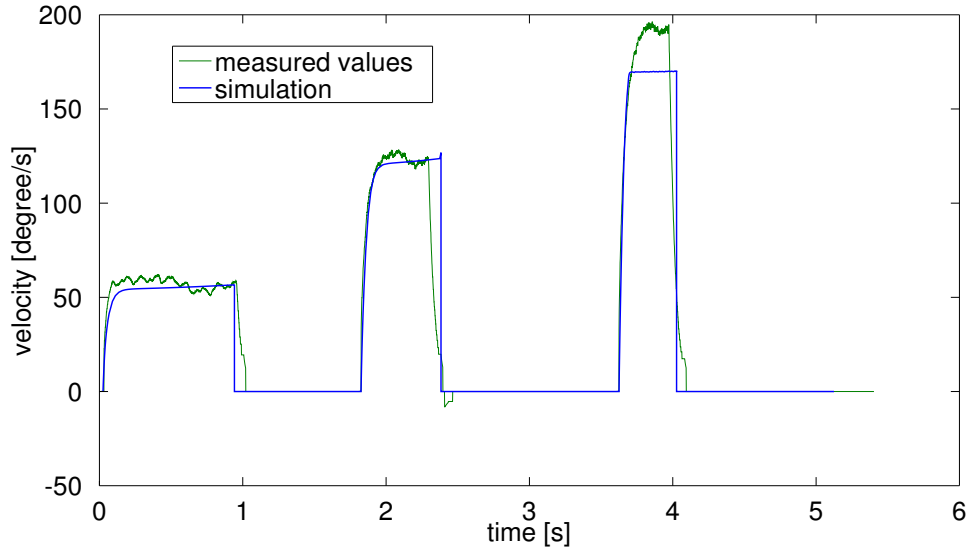


FIGURE H.3: Second verification of base joint 1: The measured values (in green) show a braking phase due to the elastic belt while the simulation (in blue) sets the velocity to zero when the finger reaches the border of movement range. The shown PWM signal are 1500, 2500 and 3500. The biggest difference between simulation and measurement is for a signal of 3500

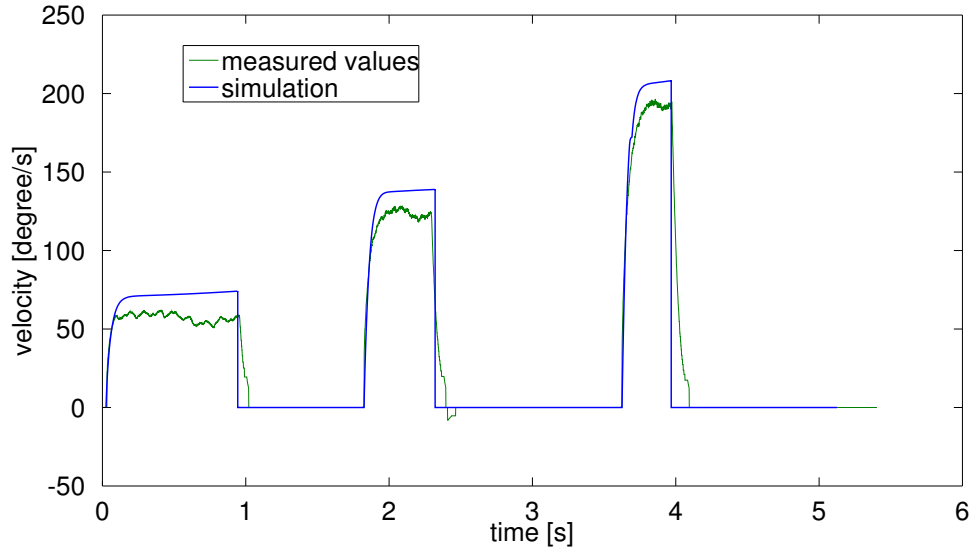


FIGURE H.4: Third verification of base joint 1: The measured values (in green) show a braking phase due to the elastic belt while the simulation (in blue) sets the velocity to zero when the finger reaches the border of movement range. The shown PWM signal are 1750 2750 and 3750.

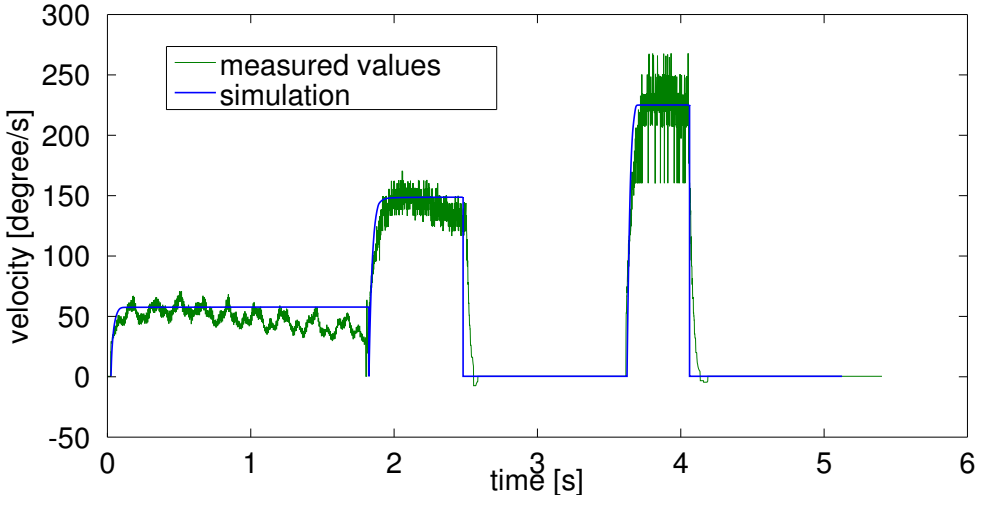


FIGURE H.5: Second verification of distal joint: The measured values (in green) show a braking phase due to the elastic belt while the simulation (in blue) sets the velocity to zero when the finger reaches the border of movement range. The shown PWM signal are 1500 2500 and 3500. As shown in the figure, the finger did not reach the end of movement range for a PWM signal of 1500.

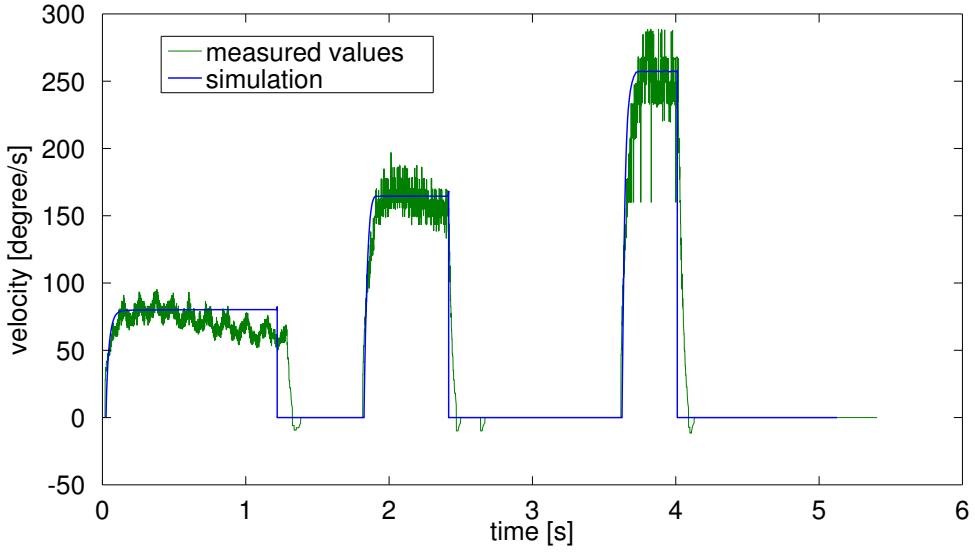


FIGURE H.6: VThird verification of distal joint: The measured values (in green) show a braking phase due to the elastic belt while the simulation (in blue) sets the velocity to zero when the finger reaches the border of movement range. The shown PWM signal are 1750 2750 and 3750.

# Bibliography


[1] World robotics, March 2014. http://www.worldrobotics.org.

[2] J. Iqbal, A. Tahir, R. ul Islam, and Riaz un Nabi. Robotics for nuclear power plants — challenges and future perspectives. *Applied Robotics for the Power Industry (CARPI), 2012 2nd International Conference on*, 2012.

[3] G.E. Wnek and G.L. Bowlin. *Encyclopedia of Biomaterials and Biomedical Engineering - Volume 2 of 2 (Print)*. Dekker Encyclopedias Series. Taylor & Francis, 2004. ISBN 9780824755560. URL http://books.google.de/books?id=oR9QxWIVOdwC.

[4] S. Acharya, V. Aggarwal, F. Tenore, Hyun-Chool Shin, R. Etienne-Cummings, M.H. Schieber, and N.V. Thakor. Towards a brain-computer interface for dexterous control of a multi-fingered prosthetic hand. In *Neural Engineering, 2007. CNE '07. 3rd International IEEE/EMBS Conference on*, pages 200–203, May 2007. doi: 10.1109/CNE.2007.369646.

[5] March 2014. http://www2.toyota.co.jp/en/news/12/09/0921.html.

[6] T. Takahashi and T. Sakai. Teaching robot's movement in virtual reality. In *Intelligent Robots and Systems '91. 'Intelligence for Mechanical Systems, Proceedings IROS '91. IEEE/RSJ International Workshop on*, pages 1583–1588 vol.3, Nov 1991. doi: 10.1109/IROS.1991.174739.

[7] Agneta Gustus, Georg Stillfried, Judith Visser, Henrik Jörntell, and P. Patrick van der Smagt. Human hand modelling: kinematics, dynamics, applications. *Biological Cybernetics*, 106(11-12):741–755, 2012. URL http://dblp.uni-trier.de/db/journals/bc/bc106.html#GustusSVJS12.

[8] M. Grebenstein, A. Albu-Schaeffer, Thomas Bahls, M. Chalon, O. Eiberger, W. Friedl, R. Gruber, S. Haddadin, U. Hagn, R. Haslinger, H. Hoppner, S. Jorg, Mathias Nickl, Alexander Nothhelfer, F. Petit, J. Reill, N. Seitz, T. Wimbock, S. Wolf, T. Wusthoff, and G. Hirzinger. The dlr hand arm system. In *Robotics and Automation (ICRA), 2011 IEEE International Conference on*, pages 3175–3182, May 2011. doi: 10.1109/ICRA.2011.5980371.

[9] N. Hogan. Impedance control: An approach to manipulation. In *American Control Conference, 1984*, pages 304–313, June 1984.

[10] J.K. Salisbury. Active stiffness control of a manipulator in cartesian coordinates. In *Decision and Control including the Symposium on Adaptive Processes, 1980 19th IEEE Conference on*, volume 19, pages 95–100, Dec 1980. doi: 10.1109/CDC.1980.272026.

[11] L. Zollo, B. Siciliano, A. De Luca, E. Guglielmelli, and P. Dario. Compliance Control for an Anthropomorphic Robot with Elastic Joints: Theory and Experiments. *Journal of Dynamic Systems, Measurement, and Control*, 127(3):321–328, September 2005.

[12] J. Huckaby and H. Christensen. Dynamic characterization of kuka light-weight robot manipulators. *Technical Report GT-RIM-CR-2012-001*, 2012.

[13] Versaball data sheet, February 2014. http://www.empirerobotics.com/pdfs/Empire_Robotics_Kit_Sheet.pdf.

[14] T. Ejima, K. Ohara, T. Takubo, Y. Mae, T. Tanikawa, and T. Arai. Design of a compact 3-dof microhand system with large workspace. In *Micro-NanoMechatronics and Human Science (MHS), 2011 International Symposium on*, pages 63–68, Nov 2011. doi: 10.1109/MHS.2011.6102160.

[15] G. Palli, Gianni Borghesan, and Claudio Melchiorri. Modeling, identification, and control of tendon-based actuation systems. *Robotics, IEEE Transactions on*, 28(2): 277–290, April 2012. ISSN 1552-3098. doi: 10.1109/TRO.2011.2171610.

[16] March 2014. http://www.elumotion.com/Elu2-hand.htm.

[17] Elu-2 hand, February 2014. http://www.elumotion.com.

[18] Eh1 milano series extrinsic robotic hand basic user guide version 1.0, 2013. http://www.prensilia.com/files/support/doc/Prensilia%20EH1%20basic_10.pdf.

[19] Shadow dexterous hand technical specification. Website, 2013. http://www.shadowrobot.com/wp-content/uploads/shadow_dexterous_hand_technical_specification_E1_20130101.pdf.

[20] Shadow dexterous hand, February 2014. http://www.shadowrobot.com.

[21] March 2014. http://www.robotarab.com/wp-content/uploads/Hand-Arm-robotarab5.jpg.

[22] M. Grebenstein. *Approaching human performance: The functionality driven Awiwi robot hand*. PhD thesis, ETH Zurich, 2012.

[23] March 2014. http://www.grandecouleur-id.de/de/projekte/.

[24] M. Chalon, A. Wedler, A. Baumann, W. Bertleff, A. Beyer, J. Butterfass, M. Grebenstein, R. Gruber, F. Hacker, E. Kraemer, K. Landzettel, M. Maier, H.-J. Sedlmayr, N. Seitz, F. Wappler, B. Willberg, T. Wimboeck, G. Hirzinger, and F. Didot. Dexhand: A space qualified multi-fingered robotic hand. In *Robotics and Automation (ICRA), 2011 IEEE International Conference on*, pages 2204–2210, May 2011. doi: 10.1109/ICRA.2011.5979923.

[25] C. Preusche, D. Reintsema, K. Landzettel, and G. Hirzinger. Robotics component verification on iss rokviss - preliminary results for telepresence. In *Intelligent Robots and Systems, 2006 IEEE/RSJ International Conference on*, pages 4595–4601, Oct 2006. doi: 10.1109/IROS.2006.282165.

[26] March 2014. http://upload.wikimedia.org/wikipedia/commons/8/88/Robonaut%27s_hand.jpg.

[27] L.B. Bridgwater, C.A. Ihrke, M.A. Diftler, M.E. Abdallah, N.A. Radford, J. M. Rogers, S. Yayathi, R. S. Askew, and D.M. Linn. The robonaut 2 hand - designed to do work with tools. In *Robotics and Automation (ICRA), 2012 IEEE International Conference on*, pages 3425–3430, May 2012. doi: 10.1109/ICRA.2012.6224772.

[28] T. Mouri, H. Kawasaki, K. Yoshikawa, J. Takai, and S. Ito. Anthropomorphic Robot Hand: Gifu Hand III. volume ICCAS2002, pages 1288–1293, October 2002.

[29] H. Kawasaki and T. Komatsu. Development of an anthropomorphic robot hand driven by built-in servo-motors. *in Proc. 3rd Int. Conf. ICAM , vol. 1, 1998, pp. 215–220.*, 1998.

[30] H. Kawasaki and T. Komatsu. Mechanism design of anthropomorphic robot hand: Gifu hand i. *Robot. Mechatron., vol. 11, no. 4, pp. 269–273*, 1999.

[31] H. Kawasaki, T. Komatsu, K. Uchiyama, and T. Kurimoto. Dexterous anthropomorphic robot hand with distributed tactile sensor: Gifu hand ii. In *Systems, Man, and Cybernetics, 1999. IEEE SMC '99 Conference Proceedings. 1999 IEEE International Conference on*, volume 2, pages 782–787 vol.2, 1999. doi: 10.1109/ICSMC.1999.825361.

[32] March 2014. http://www.pressestelle.tu-berlin.de/typo3temp/pics/5/539898f3e3.jpg.

[33] J. Butterfass, M. Grebenstein, H. Liu, and G. Hirzinger. Dlr-hand ii: next generation of a dextrous robot hand. In *Robotics and Automation, 2001. Proceedings 2001 ICRA. IEEE International Conference on*, volume 1, pages 109–114 vol.1, 2001. doi: 10.1109/ROBOT.2001.932538.

[34] H. Liu, K. Wu, P. Meusel, N. Seitz, G. Hirzinger, M.H. Jin, Y.W. Liu, S.W. Fan, T. Lan, and Z.P. Chen. Multisensory five-finger dexterous hand: The dlr/hit hand ii. In *Intelligent Robots and Systems, 2008. IROS 2008. IEEE/RSJ International Conference on*, pages 3692–3697, Sept 2008. doi: 10.1109/IROS.2008.4650624.

[35] March 2014. http://www.dlr.de/rm/desktopdefault.aspx/tabid-4789/7945_read-12721/.

[36] M.V. Liarokapis, P.K. Artemiadis, and K.J. Kyriakopoulos. Telemanipulation with the dlr/hit ii robot hand using a dataglove and a low cost force feedback device. In *Control Automation (MED), 2013 21st Mediterranean Conference on*, pages 431–436, June 2013. doi: 10.1109/MED.2013.6608758.

[37] G. Salvietti, L. Meli, G. Gioioso, M. Malvezzi, and D. Prattichizzo. Object-based bilateral telemanipulation between dissimilar kinematic structures. In *Intelligent Robots and Systems (IROS), 2013 IEEE/RSJ International Conference on*, pages 5451–5456, Nov 2013. doi: 10.1109/IROS.2013.6697145.

[38] M.V. Liarokapis, P.K. Artemiadis, and K.J. Kyriakopoulos. Mapping human to robot motion with functional anthropomorphism for teleoperation and telemanipulation with robot arm hand systems. In *Intelligent Robots and Systems (IROS), 2013 IEEE/RSJ International Conference on*, pages 2075–2075, Nov 2013. doi: 10.1109/IROS.2013.6696638.

[39] N.Y. Lii, Zhaopeng Chen, B. Pleintinger, C.H. Borst, G. Hirzinger, and A. Schiele. Toward understanding the effects of visual- and force-feedback on robotic hand grasping performance for space teleoperation. In *Intelligent Robots and Systems (IROS), 2010 IEEE/RSJ International Conference on*, pages 3745–3752, Oct 2010. doi: 10.1109/IROS.2010.5650186.

[40] Zhaopeng Chen, N.Y. Lii, T. Wimboeck, Shaowei Fan, Minghe Jin, C.H. Borst, and Hong Liu. Experimental study on impedance control for the five-finger dexterous robot hand dlr-hit ii. In *Intelligent Robots and Systems (IROS), 2010 IEEE/RSJ International Conference on*, pages 5867–5874, Oct 2010. doi: 10.1109/IROS.2010.5649356.

[41] A. Albu-Schaeffer and G. Hirzinger. Cartesian impedance control techniques for torque controlled light-weight robots. In *Robotics and Automation, 2002. Proceedings. ICRA '02. IEEE International Conference on*, volume 1, pages 657–663 vol.1, 2002. doi: 10.1109/ROBOT.2002.1013433.

[42] R. Boughdiri, H. Bezine, N. K.M'Sirdi, A. Naamane, and A. M.Alimi. Dynamic modeling of a multi-fingered robot hand in free motion. *8th International Multi-Conference on Systems, Signals and Devices*, 2011.

[43] D. Hirano, Y. Fujii, S. Abiko, R. Lampariello, K. Nagaoka, and K. Yoshida. Vibration suppression control of a space robot with flexible appendage based on simple dynamic model. In *Intelligent Robots and Systems (IROS), 2013 IEEE/RSJ International Conference on*, pages 789–794, Nov 2013. doi: 10.1109/IROS.2013.6696441.

[44] Zhong-Yu Zhao, Wen-Fang Xie, and Wen-Hong Zhu. Fuzzy optimal control for harmonic drive system with friction variation with temperature. In *Mechatronics and Automation, 2007. ICMA 2007. International Conference on*, pages 3321–3326, Aug 2007. doi: 10.1109/ICMA.2007.4304095.

[45] M. Callegari, F. Cannella, and G. Ferri. Multi-body modelling of timing belt dynamics. *Proceedings of the Institution of Mechanical Engineers*, 2002.

[46] B. Stojanović, N. Miloradović, N. Marjanović, M. Blagojević, and L. Ivanović. Length variation of toothed belt during exploitation. *Strojniški vestnik - Journal of Mechanical Engineering 57(2011)9, 637-647*, 2011.

[47] March 2014. http://images.vogel.de/vogelonline/bdb/398800/398890/sourceimage.jpg.

[48] May 2014. http://www.youtube.com/watch?v=nj1vO3cP7ug.

[49] T. Tuttle. Understanding and modeling the behavior of a harmonic drive gear transmission. Master's thesis, MIT Department of Mechanical Engineering and MIT Artificial Intelligence Laboratory, 1992.

[50] T.D. Tuttle and W. Seering. Modeling a harmonic drive gear transmission. In *Robotics and Automation, 1993. Proceedings., 1993 IEEE International Conference on*, pages 624–629 vol.2, May 1993. doi: 10.1109/ROBOT.1993.291889.

[51] J.J. Craig. *Introduction to Robotics: Mechanics and Control*. Addison-Wesley series in electrical and computer engineering: control engineering. Pearson Education, Incorporated, 2005. ISBN 9780201543612. URL http://books.google.de/books?id=MqMeAQAAIAAJ.

[52] Richard M. Murray, S. Shankar Sastry, and Li Zexiang. *A Mathematical Introduction to Robotic Manipulation*. CRC Press, Inc., Boca Raton, FL, USA, 1st edition, 1994. ISBN 0849379814.

[53] Tsuneo Yoshikawa. *Foundations of Robotics: Analysis and Control*. MIT Press, Cambridge, MA, USA, 1990. ISBN 0-262-24028-9.

[54] B. Tibor, V. Fedak, and F. Durovsky. Modeling and simulation of the bldc motor in matlab gui. In *Industrial Electronics (ISIE), 2011 IEEE International Symposium on*, pages 1403–1407, June 2011. doi: 10.1109/ISIE.2011.5984365.

[55] maxon dc motor und maxon ec motor, 2011. http://imperia.mi-verlag.de/imperia/md/upload/article/606ag0107_07_wichgtiges_dc_ec_motoren_d.pdf.

[56] Ec 20 flat 20 mm, brushless, 5 watt, 2009. http://www.electromate.com/ftp/public/Maxon%20Product%20Catalogs/Maxon%20Catalog%202009-2010/186.pdf.

[57] Präzisions-drehmomentsensor rotierend, berührungslos drehwinkel- und drehzahlmessung optional typ 8661. Website, 2014. http://burster.de/uploads/tx_productkat/8661_DE.pdf.

[58] Typ 513, 2014. http://www.mobac.de/pdf/perm/perm-513.pdf.

[59] Ruderman M. *Zur Modellierung und Kompensation dynamischer Reibung in Aktuatorsystemen*. PhD thesis, Technische Universität Dortmund, 2012.

[60] J. Badger1, A. Hulse, R. Taylor, A. Curtis, D. Gooding1, and A. Thackston. Model-based robotic dynamic motion control for the robonaut 2 humanoid robot. *Hummanoids 2013*, 2013.

[61] R. Stribeck. The key qualities of sliding and roller bearings. *VDI Zeitschrift, 46(36–38):1341–1348,1432–1438,1463–1470, 1902*, 2007.